Experimental and theoretical assessment of the mechanism and site requirements for ketonization of carboxylic acids on oxides

Shuai Wang, Enrique Iglesia *

Department of Chemical and Biomolecular Engineering, University of California at Berkeley, Berkeley, CA 94720, USA

ABSTRACT

Ketonization of carboxylic acids removes O-atoms and forms new C—C bonds, thus providing routes from sustainable carbon feedstocks to fuels and chemicals. The elementary steps involved and their kinetic relevance, as well as the number and nature of the active sites on active TiO_2 and ZrO_2 catalysts, remain matters of active discourse. Here, site titrations demonstrate the requirement for coordinatively-unsaturated M-O-M sites (M = Ti, Zr) with specific geometry and intermediate acid-base strength. The measured site densities allow rigorous reactivity comparisons among catalysts based on turnover rates and activation free energies, as well as the benchmarking of mechanistic proposals against theoretical assessments. Kinetic, isotopic, spectroscopic, and theoretical methods show that C_2—C_4 acids react on anatase TiO_2 via kinetically-relevant C—C coupling between 1-hydroxy enolate species and coadsorbed acids bound at vicinal acid-base pairs saturated with active monodentate carboxylates. Smaller Ti—Ti distances on rutile TiO_2 lead to the prevalence of unreactive bidentate carboxylates and lead to its much lower ketonization reactivity than anatase. The prevalent dense monolayers of chemisorbed acid reactants reflect their strong binding at acid-base pairs and their stabilization by H-bonding interactions with surface OH groups derived from the dissociation of the carboxylic acids or the formation of 1-hydroxy enolates; these interactions also stabilize C—C coupling transition states preferentially over their carboxylate precursors; high coverages favor sequential dehydration routes of the α-hydroxy-γ-carboxy-alk oxide C—C coupling products over previously unrecognized concerted six-membered-ring transition states. Infrared spectra show that ubiquitous deactivation, which has precluded broader deployment of ketonization in practice and unequivocal mechanistic inquiries, reflects the gradual formation of inactive bidentate carboxylates. Their dehydration to ketene-like gaseous species is faster on anatase TiO_2 than on ZrO_2 and allows the effective scavenging of bidentate carboxylates via ketene hydrogenation to alkanals/alkanols on a Cu function present within diffusion distances. These strategies make anatase TiO_2, a more effective catalyst than ZrO_2, in spite of its slightly lower initial turnover rates. This study provides details about the mechanism of ketonization of C_2—C_4 carboxylic acids on TiO_2 and a rigorous analysis of the sites required and of active and inactive bound species on TiO_2 and ZrO_2. The preference for specific distances and for intermediate acid-base strength in M-O-M species is consistent with the structure and energy of the proposed transition states and intermediates; their relative stabilities illustrate how densely-covered surfaces, prevalent during ketonization catalysis, represent an essential requirement for the achievement of practical turnover rates.

© 2016 Published by Elsevier Inc.

1. Introduction

Carboxylic acids form new C—C bonds via bimolecular ketonization reactions to give alkanones, CO_2, and H_2O [1]:

$$R_1COOH + R_2COOH \rightarrow R_1C(=O)R_2 + CO_2 + H_2O \quad (R_1, R_2 = alkyl) \quad (1)$$
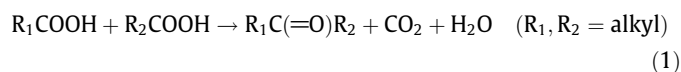
Such reactions remove three O-atoms and form a new C—C bond from two acid molecules, thus providing an attractive route for oxygen removal using the C-atoms within reactants, instead of added H_2, in upgrading biomass-derived feedstocks into fuels and chemicals [2–6]. The alkanone products can be used in subsequent aldol condensation reactions to increase their chain length and remove additional O-atoms [7,8].

Ketonization is catalyzed by metal oxides (e.g. MgO, BaO, MnO_2, CeO_2, ZrO_2, and TiO_2) [6–22], with ZrO_2 and TiO_2 among the most effective oxides [2,3]. Ketonization elementary steps and their

* Corresponding author.
  E-mail address: iglesia@berkeley.edu (E. Iglesia).

kinetic relevance on oxides remain controversial subjects of inquiry, because of a dearth of detailed kinetic, isotopic, and spectroscopic data at conditions of strict kinetic control and also because of limited theoretical confirmation for the diverse types of pathways proposed [2,3,9,17,19].

Ketonization requires the presence of a H-atom at an α-position with respect to the —COOH group in one of the acid reactants [2]. For instance, pivalic acid (C(CH$_3$)$_3$COOH), which lacks an α-H-atom, reacts with valeric acid (CH$_3$(CH$_2$)$_3$COOH, two α-H-atoms) to form 2,2-dimethyl heptan-3-one in cross-ketonization, but cannot undergo self-ketonization to form 2,2,4,4-tetramethyl pentan-3-one [19]. Similarly, aldol condensation reactions of carbonyl compounds require two α-H-atoms in one of the reactants, because such reactions involve enolate species formed by cleavage of α-C—H bonds and subsequent dehydration of aldols formed to α, β-unsaturated carbonyl compounds [23,24]. These C—H bonds exhibit lower heterolytic dissociation energies than those at other locations within the molecules; their cleavage is mediated by acid-base pairs of intermediate strength, which stabilize the transition states required for enolate formation [5,7,24]. The enolates formed from the carbonyl reactants then couple with another carbonyl species to form unstable aldols with a new C—C bond, which subsequently dehydrate to α,β-unsaturated carbonyl aldol condensation products (Scheme 1).

It seems plausible that the ketonization of carboxylic acids is also mediated by enolate-like species, in this case, in the form of 1-hydroxy enolates. The species formed from C—C bond formation via reactions of 1-hydroxy enolates with another acid reactant ultimately decompose via CO$_2$ and H$_2$O elimination, instead of the H$_2$O elimination route in condensation reactions, because neither dehydration nor decarboxylation steps alone can form stable products (Scheme 1). ^{13}C tracer studies show that the CO$_2$ molecule forms from the carboxyl group in the acid reactant that undergoes α-C—H bond cleavage and then nucleophilically attacks a coadsorbed acid reactant [10,25]; this is consistent with 1-hydroxy enolates as reaction intermediates, but excludes ketene-mediated routes, which would form CO$_2$ from the carboxyl group in the coadsorbed acid instead of that in the acid that undergoes α-C—H bond cleavage [2,9].

Here, we report turnover rates and selectivities for ketonization of C$_2$—C$_4$ carboxylic acids on anatase and rutile TiO$_2$ (TiO$_2$(a), TiO$_2$(r)) and on monoclinic and tetragonal ZrO$_2$ (ZrO$_2$(m), ZrO$_2$(t)). This study exploits the benefits of gaseous H$_2$ and a Cu function to confer unprecedented catalyst stability, thus allowing detailed mechanistic inquiries on stable catalysts. These mechanistic studies include kinetic, isotopic, spectroscopic, and theoretical

methods, which are combined here to probe plausible ketonization elementary steps and their kinetic relevance on TiO$_2$(a), an active and stable catalyst for these reactions, and on TiO$_2$(r), the least active catalyst among those examined. A parallel examination of such ketonization pathways on ZrO$_2$ has confirmed the involvement of elementary steps similar to those reported here on TiO$_2$. Reactivities are reported here as ketonization turnover rates, using the number of acid-base M—O (M = Ti, Zr) pairs determined by titration with propanoic acid during catalysis; such rates allow comparisons of the intrinsic properties of acid-base pairs on different metal oxides and rigorous benchmarking of theoretical methods against experiments. These data provide compelling evidence for the involvement of acid-base pairs in ketonization steps and for the consequences of their acid-base properties and geometry on the intrinsic ketonization reactivity of metal oxide surfaces.

These experimental and theoretical methods show that acid-base pairs are saturated with monodentate carboxylates on TiO$_2$(a) and with bidentate carboxylates on TiO$_2$(r) during ketonization catalysis. Monodentate carboxylate structures form from dissociation of the carboxylic acid on a Ti—O pair via interactions of their two O-atoms with the Ti center and the abstracted proton bound at the O site, while bidentate configurations place the two O-atoms at Ti centers of two vicinal Ti—O pairs. Such near-saturation coverages by acid-derived species prevent the re-adsorption and secondary condensation of primary alkanone products along the catalyst bed, thus maintaining the high ketonization selectivities typical of TiO$_2$ (and ZrO$_2$) catalysts. Infrared spectra during catalysis show that monodentate carboxylates and molecularly adsorbed acids are reactive intermediates on TiO$_2$(a) and TiO$_2$(r) surfaces, respectively; bidentate carboxylates, in contrast, act as unreactive spectators on both surfaces. These bidentate carboxylates can be scavenged via hydrogenation of ketene, present as trace gaseous species in equilibrium with bidentate carboxylates; such reactions are mediated by a Cu function present within diffusion distances from TiO$_2$ surfaces, leading to much slower deactivation for TiO$_2$ (and ZrO$_2$) catalysts when H$_2$ and Cu are present.

The form of the measured rate equations for all carboxylic acids, the observed (H/D) kinetic isotope effect values near unity, the infrared evidence for near saturation coverages of monodentate or bidentate carboxylates, and the effects of alkyl substituents on ketonization turnover rates are consistent with C—C bond formation between a 1-hydroxy enolate and a coadsorbed acid as the sole kinetically-relevant step. These conclusions are confirmed by DFT treatments on densely-covered TiO$_2$(a) and TiO$_2$(r) surfaces, which lead to activation free energy barriers and kinetic isotope effects in excellent agreement with experiments, while also

(a) Aldol condensation
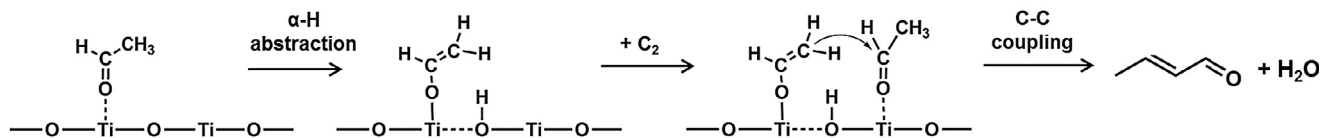
(b) Ketonization
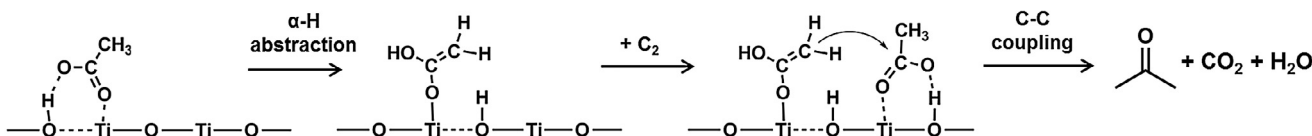
Scheme 1. Analogous elementary steps involved in ethanal condensation and ethanoic acid ketonization on acid-base pairs (shown for TiO$_2$ catalysts as an illustrative example).

confirming the prevalence of monodentate or bidentate carboxylates. High coverages of monodentate carboxylates are essential for ketonization turnovers on $TiO_2(a)$, because the kinetically-relevant C—C coupling transition state (TS) is stabilized by H-bonding interactions with vicinal surface OH groups, formed upon dissociation of coadsorbed acids to carboxylates; such stabilization decreases the free energy difference between the C—C coupling TS and the two monodentate carboxylate precursors. The Ti—Ti distances in Ti—O—Ti structures are shorter on $TiO_2(r)$ than on $TiO_2(a)$ surfaces. Such shorter distances bring more effective orbital overlap between Ti centers and O-atoms in bidentate carboxylates, leading to their prevalence over the monodentate modes, for which closer Ti—Ti centers lead to steric repulsion. Steric hindrance also destabilizes C—C coupling TS structures on $TiO_2(r)$ surfaces, rendering such surfaces essentially inactive in ketonization catalysis. The intermediacy of monodentate carboxylates present at near saturation coverages, the unreactive nature of bidentate carboxylates, and the kinetic relevance of the C—C coupling TS involving 1-hydroxy enolates and coadsorbed acid reactants appear to be general mechanistic features of ketonization reactions on practical oxide catalysts.

2. Methods

2.1. Catalyst preparation and characterization

Anatase TiO_2 ($TiO_2(a)$, 99.7%, 240 $m^2 g^{-1}$, Alfa Aesar) and rutile TiO_2 ($TiO_2(r)$, 99.5%, 160 $m^2 g^{-1}$, Aldrich) were treated in flowing air (99.999%, 1.67 $cm^3 g^{-1} s^{-1}$, Praxair) by heating to 673 K (at 0.167 $K s^{-1}$) and holding for 3 h. Monoclinic ZrO_2 ($ZrO_2(m)$, 131 $m^2 g^{-1}$) was prepared using hydrothermal methods [26]. ZrO $(NO_3)_2$ ($ZrO(NO_3)_2 \cdot 2H_2O$, 99.5%, Sigma-Aldrich) and urea (99%, Aldrich) were dissolved in 60 cm^3 deionized water (0.40 mmol cm^{-3} Zr^{4+}, urea/Zr^{4+} = 10 mole). This solution was placed in a Teflon-lined stainless-steel autoclave (100 cm^3) and held stagnant at 433 K for 20 h under its autogenous pressure. The resulting solids were washed with deionized water until the filtrate reached a neutral pH, then treated in stagnant ambient air at 383 K (0.167 $K s^{-1}$) overnight and in flowing air (1.67 $cm^3 g^{-1} s^{-1}$, 99.999%, Praxair) at 673 K (0.167 $K s^{-1}$ heating rate, 4 h hold). Tetragonal ZrO_2 ($ZrO_2(t)$, 167 $m^2 g^{-1}$) was prepared via hydrolysis of $ZrOCl_2$ ($ZrOCl_2 \cdot 8H_2O$, 99.5%, Sigma-Aldrich) in an aqueous solution (0.40 mmol cm^{-3} Zr^{4+}; 333 K) at a constant pH of 10 adjusted by 5.0 M NH_4OH (99.99%, Sigma-Aldrich) [27]. The precipitate was washed with deionized water until the rinse solution was free of Cl^- ions, as determined using 0.2 mmol cm^{-3} aqueous $AgNO_3$ (>99.0%, Sigma-Aldrich). The samples were then treated at 383 K (0.167 $K s^{-1}$) overnight in stagnant ambient air and at 723 K (0.167 $K s^{-1}$) for 2 h in flowing air (1.67 $cm^3 g^{-1} s^{-1}$, 99.999%, Praxair). The identity and phase purity of these ZrO_2 samples were examined by powder X-ray diffraction (XRD) measurements (Cu Kα radiation, λ = 0.15418 nm, 40 kV, 40 mA, Bruker D8 Advance; diffractograms shown in Fig. S1 of Supporting Information (SI)).

H_2 and Cu/SiO_2 catalysts (ca. 20 wt.% Cu) were used to improve the stability of TiO_2 and ZrO_2 ketonization catalysts. The Cu-based catalysts were prepared using homogeneous deposition-precipitation methods [24]. $Cu(OH)_2$ was deposited onto colloidal silica (30 wt.%, LUDOX SM-30) from an aqueous solution of Cu $(NO_3)_2$ ($Cu(NO_3)_2 \cdot 2.5H_2O$, 99.99%, Sigma-Aldrich) via urea hydrolysis ($CO(NH_2)_2$, 99%, Aldrich) at 363 K (urea/Cu^{2+} = 3 mole). The resulting suspension was kept at 363 K (0.167 $K s^{-1}$) for 20 h while stirring (12 Hz) and then filtered and washed with deionized water until the filtrate gave a neutral pH value. The recovered powders were treated in stagnant ambient air by heating to 383 K (at

0.167 $K s^{-1}$) and holding overnight and in flowing dry air (1.67 $cm^3 g^{-1} s^{-1}$, 99.999%, Praxair) by heating to 723 K (at 0.167 $K s^{-1}$) and holding for 5 h. These samples were then treated in flowing 10% H_2/He (5.56 $cm^3 g^{-1} s^{-1}$, 99.999%, Praxair) at 573 K (0.033 $K s^{-1}$) for 2 h, and passivated in flowing 1% O_2/He (0.83 $cm^3 g^{-1} s^{-1}$, 99.999%, Praxair) at ambient temperature for 1 h before exposure to ambient air. The mean Cu crystallite size (d) in Cu/SiO_2 (7.9 nm) [24] was measured from the breadth of the most intense (111) reflection in diffractograms (2θ = 43.3°) using the Scherrer equation and Cu Kα radiation (0.15418 nm wavelength).

2.2. Catalytic rate measurements

The reactions of gaseous C_2–C_4 carboxylic acids (ethanoic acid (CH_3COOH, >99.7%, Sigma-Aldrich), propionic acid (C_2H_5COOH, >99.5%, Sigma-Aldrich), and butanoic acid (C_3H_7COOH, >99%, Sigma-Aldrich)) were carried out in an isothermal packed-bed reactor (1.0 cm I.D.) with plug-flow hydrodynamics at temperatures between 503 K and 533 K. Experiments were carried out on $TiO_2(a)$, $TiO_2(r)$, $ZrO_2(m)$, and $ZrO_2(t)$ and on their respective physical mixtures with 20 wt.% Cu/SiO_2 co-catalysts (oxide/(Cu/SiO_2) = 0.5–2 mass); these mixtures were prepared by crushing and mixing the mixtures with a mortar and pestle and then pressed into wafers, crushed, and sieved to retain 125–180 μm aggregates. The mixtures were then treated in flowing 10% H_2/He (5.56 $cm^3 g^{-1} s^{-1}$, 99.999%, Praxair) by heating to 543 K (at 0.0833 $K s^{-1}$) and holding for 2 h within the reactor before catalytic measurements. Liquid carboxylic acids were introduced using a syringe pump (Cole Parmer, 74900 series) at 433 K into a flow of H_2-He mixtures (20 kPa H_2, 99.999%, Praxair) metered using electronic mass flow controllers (Porter, Inc.). All lines were kept at 433 K to prevent condensation of reactants and products. Isotopic data were obtained using the same procedures and ethanoic acid-d_4 (CD_3COOD, >99%, Sigma-Aldrich) and D_2 (>99%, Praxair) as reactants.

Reactant and product concentrations were determined by on-line gas chromatography (Agilent 6890). Carboxylic acids, anhydrides, alkanones, and other oxygenates were detected by a flame ionization detector after separation in a capillary column (Agilent, HP-1, methyl silicone, 50 m, 0.32 mm ID × 1.05 μm). H_2, H_2O, CO, and CO_2 were detected by measuring thermal conductivity after chromatographic separation in a packed column (Porapak-Q, 4.8 m, 80–100 mesh). Molecular speciation was confirmed using known standards and mass spectrometry (HP 5972 mass spectrometer). A carbon basis was used to calculate all conversions and selectivities. For catalytic rate measurements, reactant conversions were kept below 5% to ensure the absence of axial reactant concentration gradients.

2.3. Titration of acid-base pairs during catalysis

Acid-base pairs on oxide surfaces can be titrated with carboxylic acids during aldol condensation, because acids strongly bind at such pairs and convert via ketonization at much lower rates than aldol condensation turnovers of carbonyl compounds [24]. These acid-base pairs are involved in both condensation and ketonization reactions, as shown in this study, thus allowing the rigorous reporting of the reactivity of each catalyst as turnover rates. These titrations were carried out on $TiO_2(a)$, $TiO_2(r)$, $ZrO_2(m)$, and $ZrO_2(t)$ catalysts using propanoic acid titrants (20 Pa) during acetone condensation reactions (0.8 kPa, 453 K) [24]. The titrant and product concentrations in the effluent were measured using the chromatographic protocols described above. The number of accessible acid-base pairs on the oxides was determined from the amount of adsorbed propionic acid required to fully suppress con-

densation rates and the specific titrant stoichiometry inferred from infrared evidence and DFT treatments for each oxide. These studies showed that $TiO_2(a)$ favors dissociated acids bound in a monodentate form on a single Ti—O pair via respective interactions of the two O-atoms in the formed carboxylates with the Ti center and the abstracted proton bound at the O-atom in the Ti—O pair (Sections 3.3 and 3.4), leading to a titrant stoichiometry of one acid per Ti—O pair. In contrast, $TiO_2(r)$ (Sections 3.3 and 3.4), $ZrO_2(m)$ [3], and $ZrO_2(t)$ [3] favor dissociated acids interacting with two vicinal M—O pairs (M = Ti, Zr) via interactions of each of the two O-atoms in the carboxylate structures with one of the M centers and interaction of the abstracted H-atom and one of the lattice O-atoms, to give a stoichiometry of one acid for each two M—O pairs.

Measured titration values for these TiO_2 and ZrO_2 oxides are in reasonable agreement with their low-index-plane site densities except for $TiO_2(r)$ (Table 1). The fast prevalent deactivation of $TiO_2(r)$, caused by desorption hurdles of condensation products, accounts for its lower measured Ti—O pair densities [24]. These densities of acid-base pairs (Table 1) were used to report ketonization reactivity as turnover rates, a measure of intrinsic reactivity that allows rigorous comparisons among oxides and between theory and experiment for each oxide catalyst.

2.4. Infrared spectroscopy measurements

Transmission infrared (IR) spectra were measured using a Nicolet 8700 FT-IR spectrometer equipped with a Hg-Cd-Te (MCT) detector. Samples were pressed into self-supporting wafers (5–15 mg cm^{-2}) and placed in a cell with KBr windows. The samples were treated at 573 K (0.0833 K s^{-1}) in He (5.56 cm^3 g^{-1} s^{-1}, 99.999%, Praxair) for 2 h and then cooled to 523 K before collecting spectra. Ethanoic acid (>99.7%, Sigma-Aldrich; 0.2–1.6 kPa) was injected using a syringe pump using the same procedures as for rate measurements (Section 2.2). All spectra were collected by averaging 64 scans in the 4000–650 cm^{-1} range with a 2 cm^{-1} resolution and normalized by the C=O stretching band intensity of gaseous ethanoic acid (1900–1600 cm^{-1}) at 1.6 kPa.

2.5. Density functional theory methods

Theoretical treatments of the elementary steps involved in ketonization of ethanoic acid on $TiO_2(a)$ and $TiO_2(r)$ surfaces were carried out using periodic plane-wave density functional theory (DFT) methods [31–34] with the Perdew-Burke-Ernzerhof (PBE) exchange-correlation functional [35,36] as implemented in the Vienna ab initio simulation package (VASP). The $3p^64s^23d^2$, $2s^22p^4$, $2s^22p^2$, and $1s^1$ electrons were treated explicitly for Ti, O, C and H atoms; core electrons were treated using projector augmented-wave (PAW) pseudopotentials with an energy cutoff of 400 eV [37,38]. The Monkhorst-Pack sampling method [39] was used to generate the k-mesh for integration of the first Brillouin zone (i.e. $4 \times 4 \times 4$ for bulk structures of $TiO_2(a)$ and $TiO_2(r)$ and $4 \times 4 \times 1$ for surfaces of $TiO_2(a)$ and $TiO_2(r)$). The energy between successive self-consistent iterations was converged to

1×10^{-6} eV, while the structures were optimized until forces were below 0.05 eV Å^{-1}.

The known structures of crystalline $TiO_2(a)$ (tetragonal, $I4_1$/amd, $a = b = 0.383$ nm, $c = 0.961$ nm) [40] and $TiO_2(r)$ (tetragonal, $P4_2$/mnm, $a = b = 0.458$ nm, $c = 0.295$ nm) [40] were used as the starting point for energy optimizations of bulk $TiO_2(a)$ and $TiO_2(r)$. The DFT-optimized lattice vectors of $TiO(a)$ ($a = b = 0.378$ nm, $c = 0.950$ nm) and $TiO(r)$ ($a = b = 0.464$ nm, $c = 0.299$ nm) determined from fitting of energy-volume data with the Birch-Murnaghan equation of state [41] were both 1.2% larger than for the respective known structures. $TiO_2(a)$ (1 0 1) and $TiO_2(r)$ (1 1 0) surfaces are the most stable exposed ones for the respective TiO_2 phases [40] and were chosen as the model surfaces. For the $TiO_2(a)$ (1 0 1) surface, 1×2, 1×4, 2×3, and 1×8 supercells were constructed in order to describe ketonization elementary reactions at 1/8, 1/6, 1/4, 1/3, 1/2, and 1 ethanoic acid monolayers (ML) (1–2 acid reactants per supercell), whereas 1×2, 1×4, and 1×8 supercells were constructed and used for the $TiO_2(r)$ (1 1 0) surface correspondingly. Each ($m \times n$) supercell contained four $Ti_{m \times n}O_{2 \times m \times n}$ layers in the z-direction with the bottom layer fixed at its bulk position and the other layers allowed to relax to their minimum energy structures in response to the presence of adsorbed species. Periodic images were separated by 1.5 nm along the z-direction, and the dipole interaction between images along the z-direction was corrected during each geometric optimization step [42]. Grimme's D3BJ dispersion corrections were also included during the optimization processes to account for van der Waals interactions among atoms [43,44]. Adsorption free energies (ΔG_{ads}) for ethanoic acid on Ti—O pairs of $TiO_2(a)$ or $TiO_2(r)$ surfaces to form molecularly bound acids or dissociate to carboxylates are determined by

$$\Delta G_{ads} = \frac{1}{\lambda}(G_{\lambda \times acid*} - G_{TiO2-(m \times n)} - \lambda G_{acid}) \tag{2}$$

where $G_{TiO2-(m \times n)}$ is the free energy of a ($m \times n$) supercell slab of a TiO_2 surface ($m = 1$, $n = 2$–8, as described above), $G_{\lambda \times acid*}$ is the free energy of this TiO_2 slab with λ ethanoic acid molecules ($\lambda = 1$ or 2), and G_{acid} is the free energy of a gaseous ethanoic acid molecule; ΔG_{ads} thus reflects the average adsorption free energy of ethanoic acid on TiO_2 surfaces at a surface coverage of $\lambda/(m \times n)$ ML.

Nudged elastic band (NEB) [45,46] and dimer [47] methods were used to determine optimized transition state (TS) structures and energies for all elementary steps. The starting point for each TS structure was obtained using NEB methods with 8–12 images along the reaction coordinate. The electronic structures were converged self-consistently to energies of 1×10^{-5} eV using a single Γ-centered k-point, and the corresponding maximum force on each atom converged to 0.1 eV Å^{-1}. The dimer algorithm was then used to optimize the TS structure using a $4 \times 4 \times 1$ Monkhorst-Pack k-point mesh and more stringent convergence criteria for electronic energies and forces (1×10^{-6} eV and 0.05 eV Å^{-1}, respectively). A frequency analysis was used to confirm that the optimized TS structure exhibited a single imaginary frequency

Table 1
Measured acid-base pair densities and values expected from crystal structures and low-index planes for TiO_2 and ZrO_2 catalysts.

Catalyst	Crystallographic acid-base pair density[a] (nm^{-2})				Measured areal density of site pairs (nm^{-2})
$TiO_2(a)$	(1 0 1) 5.2	(1 0 0) 5.6	(0 0 1) 7.0	(0 1 0) 5.6	3.7[b]
$TiO_2(r)$	(1 1 0) 5.2	(1 0 0) 7.4	(0 0 1) 7.4	(0 1 1) 8.0	1.7[b]
$ZrO_2(m)$	(−1 1 1) 6.8	(1 1 1) 8.1	(−1 0 1) 5.7	(0 1 1) 5.3	6.0[c]
$ZrO_2(t)$	(1 0 1) 8.6	(0 0 1) 7.5	(1 0 0) 5.2	(1 1 1) 3.3	5.8[c]

[a] Selected planes are the most stable ones present on each metal oxide [28–30].
[b] Adapted from Ref. [24].
[c] Titration data shown in Section S2, SI.

characteristic of the molecular vibration along the reaction coordinate.

Vibrational frequencies for the optimized structures of reactive species and transition states were determined from the Hessian matrix using the same k-point mesh and convergence criteria for the geometric optimizations, while the bottom three layers of each unit cell were all frozen during the frequency analysis in order to reduce computational cost; these frequencies were not corrected by any factors. The enthalpies, entropies, and Gibbs free energies of reactants, transition states, and products were calculated for each elementary step from these frequencies using vibrational partition functions derived from the rigid-rotor harmonic oscillator approximation [48]. Weakly-bound adsorbates contain fewer than three low-frequency modes (<60 cm^{-1}). These modes were treated as rotations similar to gaseous molecules, instead of treating as harmonic oscillators, because the latter treatments lead to significant errors in the magnitude of the vibrational partition functions [49].

Hydroxide anion affinity (E_{HA}) for an acid site (A) is defined as the energy released from binding of a gaseous hydroxide anion (OH$^-$), initially present at non-interacting distances, onto the acid site A:

$$E_{HA} = E_{AOH^-} - E_A - E_{OH^-} \qquad (3)$$

where E_i represents the electronic energy of species i; these E_{HA} values are used as energy-based descriptors of the strength of a Lewis acid site. Proton affinity (E_{PA}) for a basic site (B) is defined in a similar way in order to describe the strength of the basic site B:

$$E_{PA} = E_{HB^+} - E_B - E_{H^+} \qquad (4)$$

where E_i represents the electronic energy of species i. These affinities for the acid-base pairs present on TiO$_2$(a) (1 0 1) surfaces were estimated using a Ti$_{40}$O$_{118}$H$_{76}$ cluster model instead of the above slab models, because dipole and quadrupole energy corrections cannot be calculated correctly for periodic systems with a net charge [42]. This cluster was extracted from a TiO$_2$(a) (1 0 1) surface with H-atoms attached to terminal O-atoms to maintain charge neutrality (structure shown in Section S3, SI). Similarly, a Ti$_{40}$O$_{120}$H$_{80}$ cluster (Section S3, SI) was constructed in order to estimate E_{HA} and E_{PA} for the Ti—O pairs present on TiO$_2$(r) (1 1 0) surfaces.

3. Results and discussion

3.1. Ketonization turnover rates of carboxylic acids on TiO$_2$ and ZrO$_2$ catalysts

Ketonization reactions of C$_2$—C$_4$ carboxylic acids (C$_n$H$_{2n-1}$COOH, n = 1–3) take place with high selectivity on anatase TiO$_2$ (TiO$_2$(a)), rutile TiO$_2$ (TiO$_2$(r)), monoclinic ZrO$_2$ (ZrO$_2$(m)), and tetragonal ZrO$_2$ (ZrO$_2$(t)) catalysts. Carbon selectivities to ketonization products were above 95% (at 9–11% acid conversion, 503–533 K, Section S4, SI), consistent with previous studies on TiO$_2$(a) [16,17] and ZrO$_2$(m) [19] catalysts. Side products include acid anhydrides, formed via intermolecular dehydration of the acid reactants, and α,β-unsaturated alkanones, formed via subsequent aldol condensation of primary alkanone products (Scheme 2). The formation of acid anhydrides is equilibrium-limited, as shown by approach to equilibrium parameters near unity for the acid-anhydride interconversion reactions on TiO$_2$(a) and TiO$_2$(r) at all conditions (Section S4, SI). Secondary aldol condensation of alkanones products is inhibited by coadsorbed monodentate or bidentate carboxylates present at near saturation coverages, as shown by the kinetic and infrared data in Sections 3.2 and 3.3.

Fig. 1a shows that ethanoic acid ketonization turnover rates (per acid-base pair) on TiO$_2$ and ZrO$_2$ surfaces decreased with time-on-stream (523 K, 1.0 kPa ethanoic acid). Initial turnover rates ($r(0)$) were obtained by extrapolation of initial rates (<1 h) to the time of initial contact with reactants. The initial slope in the semi-logarithmic data reflects the value of the first-order deactivation constant (k_d):

$$\frac{r(t)}{r(0)} = e^{-k_d t} \qquad (5)$$

where $r(t)$ is the rate at any time t. These initial turnover rates were highest on ZrO$_2$(m) and lowest on TiO$_2$(r) (Fig. 1), indicative of M (M = Ti, Zr) and O centers with different acid and basic strength and geometry on these oxide surfaces, as discussed in Section 3.4. Initial turnover rates were fivefold higher on TiO$_2$(a) than on TiO$_2$(r) at 523 K and 1.0 kPa ethanoic acid; similar rate differences were previously reported for acetone condensation turnover rates [24], for which the observed reactivity of TiO$_2$(r) surfaces was ultimately attributed to residual anatase surfaces present as minority species. The measured k_d values for TiO$_2$ and ZrO$_2$ catalysts suggest that acid-base pairs that are more active also deactivate more rapidly (Fig. 1a); such trends render TiO$_2$(a), ZrO$_2$(m), and ZrO$_2$(t) similarly effective as practical ketonization catalysts, in spite of the slightly lower initial turnover rates on TiO$_2$(a).

Initial ketonization rates and deactivation constants (k_d) were similar on TiO$_2$(a) samples treated in He or H$_2$ at 543 K for 2 h before reaction (Section S5, SI). These similarities indicate that either reduced centers do not form during the treatments, consistent with the higher temperatures typically required to form O-vacancies in TiO$_2$(a) [10], or that any reduced centers present are inconsequential for ketonization. The number of acid-base pairs measured by titration methods [24] resembles those expected from low-index crystal planes (Table 1), indicating that active centers do not reflect defects that would be present merely as minority species. Such defects may be essential in "dose-and-react" stoichiometric experiments [9], because species must be kept bound at surfaces up to the temperatures required for their reactions, a requirement that is inconsequential in the presence of gaseous reactants during steady-state ketonization turnovers.

Initial rates were essentially recovered after deactivation for 48–72 h on all TiO$_2$ and ZrO$_2$ catalysts by extended treatments in flowing He at 523 K (Section S6, SI), suggesting that the site blockage occurs via the gradual formation of unreactive species that can be desorbed slowly, but without the need for a reactive environment (i.e. H$_2$ or O$_2$ treatments). Infrared spectra showed that such unreactive residues consist of bidentate carboxylates formed via dissociative adsorption of carboxylic acids on two vicinal acid-base pairs (Scheme 3; Section 3.3); the timescale for the appearance and disappearance of bidentate carboxylate vibrational features coincides with that for deactivation and regeneration, respectively (Section 3.3). DFT treatments of ketonization elementary steps on TiO$_2$(a) and TiO$_2$(r) surfaces also indicate that bidentate carboxylates are not involved in ketonization turnovers (Section 3.4); they act instead as unreactive spectators that occupy acid-base pairs, thus rendering them inaccessible for catalytic turnovers.

Ethanoic acid ketonization rates on TiO$_2$(a) and TiO$_2$(r) catalysts remained essentially constant with time in the presence of gaseous H$_2$ and a Cu function ($k_d \leqslant 0.002$ ks^{-1}; 20 kPa H$_2$, (Cu/SiO$_2$)/oxide = 1 (mass); Fig. 1b). These conditions and catalyst mixtures led to the concurrent appearance of ethanal and ethanol, which form via hydrogenolysis of ethanoic acid or hydrogenation of its ketene derivatives (CH$_2$=C=O; from dehydration of ethanoic acid [11]) on Cu surfaces (Scheme 4). The combined formation rates of these hydrogenation products were much lower than ketonization rates (Section S7, SI). Ketonization rates of propanoic acid and
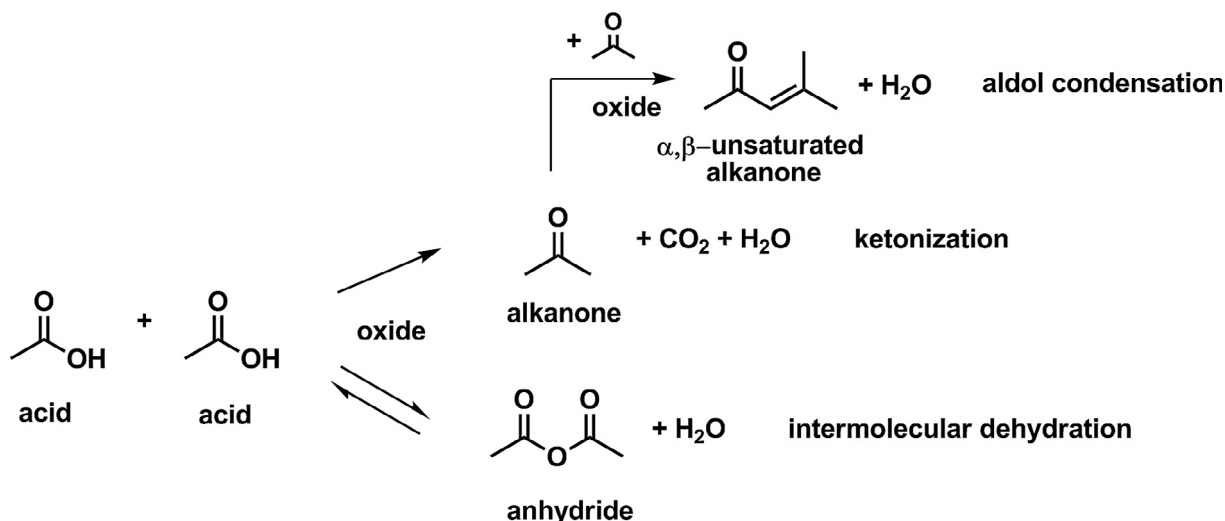
Scheme 2. Reactions of carboxylic acids catalyzed by metal oxides (shown for ethanoic acid as an illustrative example).
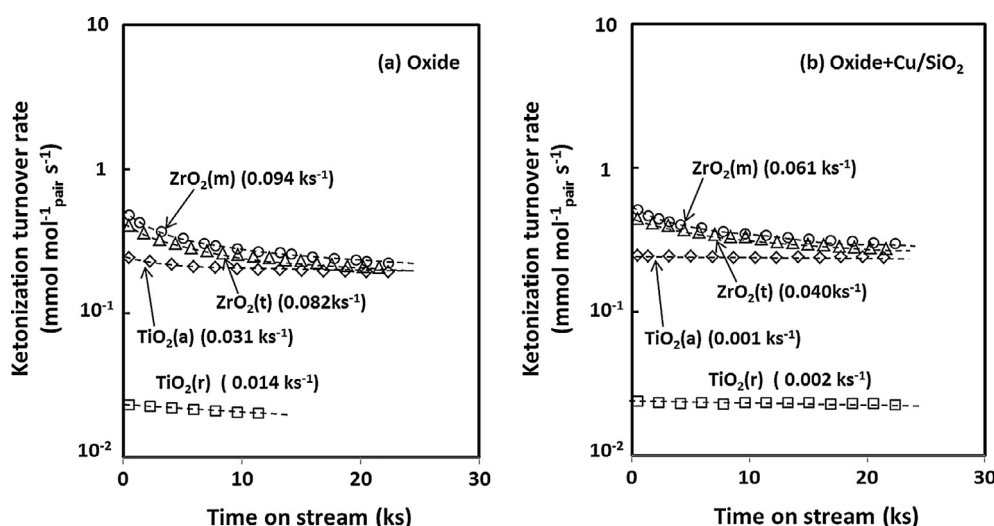

Fig. 1. Semi-logarithmic plots of ethanoic acid ketonization turnover rates (per acid-base pair measured by propanoic acid titration during catalysis; Table 1) as a function of time-on-stream (a) on TiO_2 and ZrO_2 catalysts and (b) on these catalysts as physical mixtures with Cu/SiO_2 (1:1 mass) (523 K, 1.0 kPa ethanoic acid, 20 kPa H_2 for the mixtures). First-order deactivation constants (Eq. (5)) are shown in parenthesis. Dashed curves indicate qualitative trends.
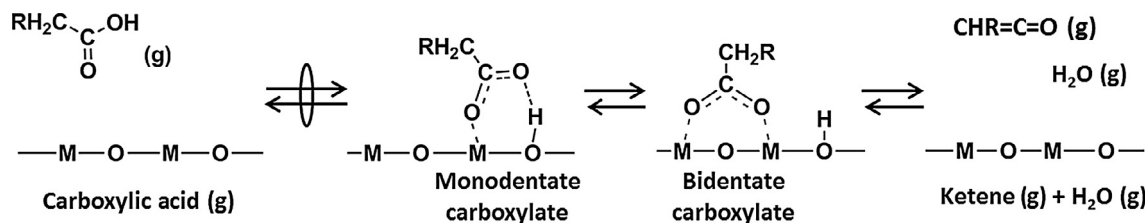

Scheme 3. Formation of surface carboxylates and gaseous ketenes on oxide surfaces during ketonization of carboxylic acids (R = H, alkyl; M = Zr, Ti).

butanoic acid were also rendered stable over time by these bifunctional strategies ($k_d \leqslant 0.002$ ks^{-1} on TiO_2(a); Fig. 2).

We surmise that the bidentate carboxylates can dehydrate to form gaseous ketenes in trace amounts (Scheme 3), as evident from DFT calculations (Section S8, SI); these ketene concentrations are set by their unfavorable formation thermodynamics and are well below detection limits. Steady-state coverages of bidentate carboxylates can thus be decreased by the continuous slow scavenging of ketene species to form ethanal and ethanol [4,50] on a Cu

function present within diffusion distances from Ti—O centers. Such scavenging into stable products prevents ketene re-adsorption and the re-formation of the unreactive bidentate carboxylates. These stable ketonization rates on TiO_2(a) and TiO_2(r) allow the rigorous assessment of the ketonization mechanism through combined kinetic and isotopic methods, as described in Section 3.2.

The deactivation of ZrO_2(m) and ZrO_2(t) catalysts in ketonization of ethanoic acid was suppressed less effectively by the gaseous
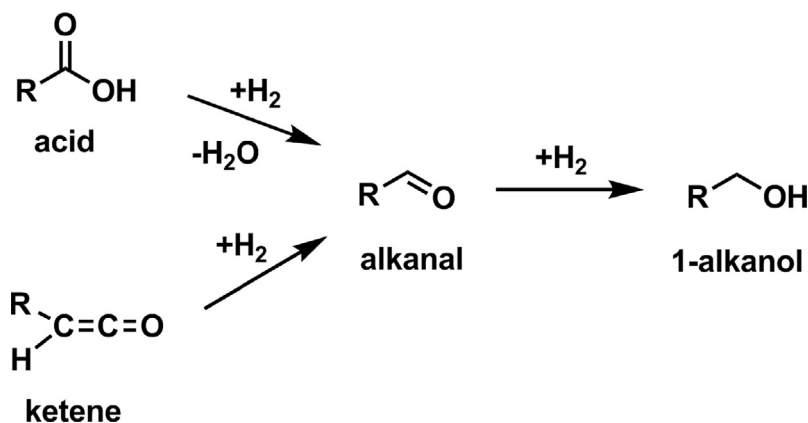
Scheme 4. Hydrogenation of carboxylic acid and ketene to alkanal and 1-alkanol (R = H, alkyl).
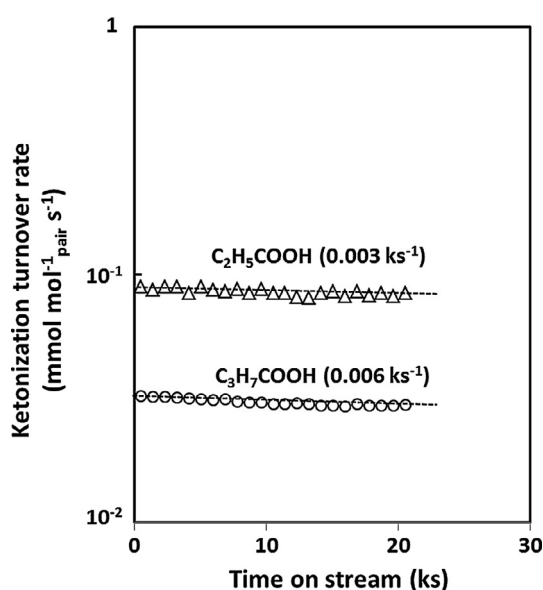
Fig. 2. Semi-logarithmic plots of ketonization turnover rates of propanoic acid and butanoic acid as a function of time-on-stream (TiO$_2$(a) + 20 wt.% Cu/SiO$_2$ (1:1 mass), 523 K, 1.0 kPa acid reactant, 20 kPa H$_2$). First-order deactivation constants (Eq. (5)) are shown in parenthesis. Dashed lines indicate qualitative exponential trends.

H$_2$ (20 kPa) and the Cu function ((Cu/SiO$_2$)/oxide = 1 mass) than on TiO$_2$(a) or TiO$_2$(r). The k_d values decreased from 0.094 to 0.061 ks^{-1} on ZrO$_2$(m) and from 0.082 to 0.040 ks^{-1} on ZrO$_2$(t) (Fig. 1), in contrast to the essential suppression of deactivation processes on TiO$_2$(a) and TiO$_2$(r) using similar strategies and conditions ($k_d \leqslant 0.002$ ks^{-1}; Fig. 1b). Higher (Cu/SiO$_2$)/oxide mass ratios did not lead to further stabilization of these ZrO$_2$ catalysts (0.060 ks^{-1} on ZrO$_2$(m) at (Cu/SiO$_2$)/oxide = 2 (mass); Section S9, SI). Such findings appear to indicate that desorption of bidentate carboxylates from ZrO$_2$(m) and ZrO$_2$(t) exhibits kinetic hurdles that inhibit their equilibration with gaseous ketene and thus the continuous scavenging of bidentate carboxylates via irreversible ketene hydrogenation on the Cu function. DFT treatments show that the conversion of bidentate carboxylates to ketenes on ZrO$_2$(m) (−1 1 1) and TiO$_2$(a) (1 0 1) surfaces is limited by the C—O bond cleavage in bidentate carboxylates; its free energy barrier is higher on ZrO$_2$(m) (−1 1 1) than on TiO$_2$(a) (1 0 1), because Zr centers on ZrO$_2$(m) are weaker Lewis acids than Ti centers on TiO$_2$(a) (Section S8, SI); as a result, the C—O cleavage TS that mediates ketene formation is less stable on ZrO$_2$(m) because its two O-atoms interact more weakly with Zr than they do with Ti centers on TiO$_2$(a).

3.2. Effects of reactant pressure on ketonization rates and implications for elementary steps and their kinetic relevance on anatase and rutile TiO$_2$

All rates reported hereinafter were obtained on stable TiO$_2$(a) and TiO$_2$(r) catalysts, present as mixtures with Cu/SiO$_2$ and in the presence of 20 kPa H$_2$ (Fig. 1b). These rates were not influenced detectably by the prevalent pressure of the ketonization products (i.e. alkanones, H$_2$O and CO$_2$; 0.02–0.2 kPa), which was varied by changes in space velocity (Section S10, SI), consistent with the weak binding of such product molecules on Ti—O pairs of moderate acid-base strength [24]. These product concentrations do not therefore appear as terms in the denominator of the ketonization rate equations derived below.

Fig. 3a shows ketonization turnover rates for ethanoic acid-d$_0$ and ethanoic acid-d$_4$ reactants as a function of their respective pressures (0.1–3.0 kPa) on TiO$_2$(a) + Cu/SiO$_2$ mixtures (523 K, 20 kPa H$_2$/D$_2$). Rates increased with increasing reactant pressure, but became less sensitive to the concentration of reactants at higher ethanoic acid pressures. Similar trends were observed for propanoic and butanoic acids (Fig. 3a) and for ethanoic acid at other temperatures (503–533 K; Fig. 3b). The nearly zero-order kinetic dependences at higher reactant pressure (>1.2 kPa) are consistent with the strong adsorption and monolayer coverages of surface carboxylates derived from acid reactants on TiO$_2$(a) at the conditions of catalysis.

A plausible sequence of ketonization elementary steps on TiO$_2$(a) is shown for the specific case of ethanoic acid in Scheme 5. This sequence leads to rate equations consistent with the rate data and isotope effects shown in Fig. 3 and with theoretical assessment of free energies for these elementary steps shown in Section 3.4. The $\vec{k}_x$ and $\overleftarrow{k}_x$ parameters in Scheme 5 represent the rate constants for the forward and reverse directions of Step x, respectively, and K_x is the corresponding equilibrium constant for each step ($K_x = \vec{k}_x / \overleftarrow{k}_x$).

These elementary steps involve the dissociation of ethanoic acid at a Ti—O pair (AcO*; monodentate carboxylate; Step 1, Scheme 5), with an O-atom in the carboxylic group bound at the Ti center and the other one H-bonded to the H-atom that is abstracted from the acid and bound at the Ti—O pair. These carboxylates can also bind to two vicinal Ti—O pairs (*AcO*; bidentate carboxylate; Step 2, Scheme 5), with each of its two O-atoms bound at one of the two Ti centers and the abstracted H-atom bound at a lattice O-atom. Infrared spectra during ketonization catalysis show that AcO* species are the most abundant surface intermediates (MASI) (Section 3.3) during ketonization on TiO$_2$(a). Ethanoic acid is not preferentially bound as bidentate carboxylate species (*AcO*), a configuration previously proposed as the prevalent MASI during
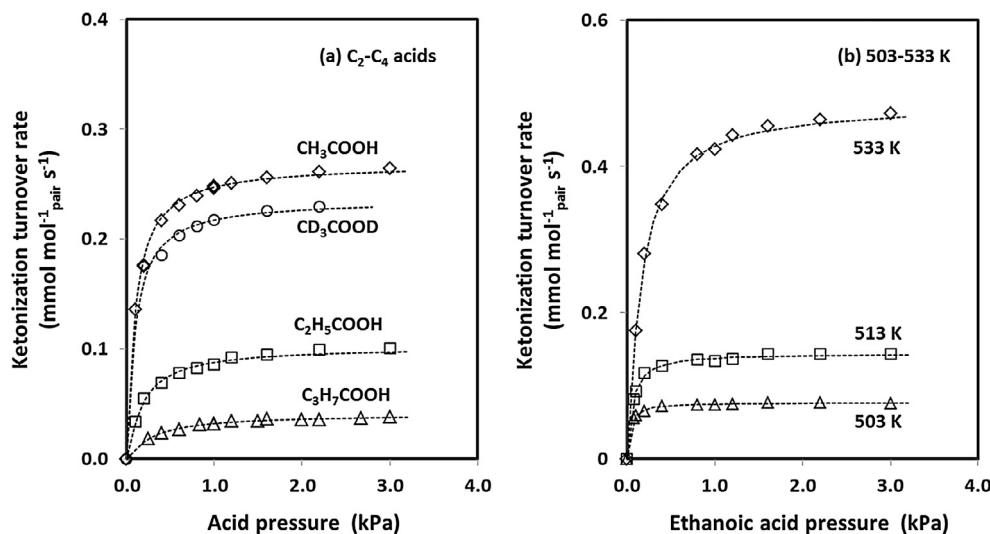
Fig. 3. Effects of reactant pressure on ketonization rates (a) for C_2—C_4 carboxylic acids at 523 K and (b) for ethanoic acid at 503–533 K (TiO$_2$(a) + 20 wt.% Cu/SiO$_2$ (1:1 mass), 20 kPa H$_2$ for undeuterated reactants, 20 kPa D$_2$ for deuterated reactants). Dashed lines represent the regressed fits to the mechanism-based functional form of Eq. (7).

catalysis and claimed as the reactive intermediate in ketonization reactions on TiO$_2$(a) [16,17,22], ZrO$_2$(m) [19,21], CeO$_2$ [14,18,22], and ZnO—Cr$_2$O$_3$ [20] based on infrared spectra of pre-adsorbed ethanoic acids at conditions removed from practical ketonization catalysis [21,22] and on DFT-derived estimates of electronic energies at low surface coverages [19]. The explicit treatments of these densely-covered surfaces and of the thermal corrections and entropy effects required for accurate energies and free energies in DFT calculations lead to the conclusion that monodentate carboxylates, instead of bidentate species, prevail as adsorbed species and that they act as the reactive intermediates in ketonization catalytic sequences on TiO$_2$ (a) (Section 3.4) and also on ZrO$_2$ surfaces, as we shall report separately.

In Scheme 5, 1-hydroxy enolates form from acids via α-C—H cleavage in AcO* species at Ti—O pairs (Step 3, Scheme 5); these enolates nucleophilically attack the carboxyl C-atom in a neighboring AcO* to form α-hydroxy γ-carboxy alkoxides containing a new C—C bond (Step 4, Scheme 5); these steps resemble those involved in aldol condensation of carbonyl compounds on acid-base pairs (Scheme 1; Ref. [24]). Aldol condensation turnovers involve cleavage of α-C—H bonds to form enolate species and subsequent C—C bond formation between the enolate and a coadsorbed carbonyl reactant bound at a vicinal Ti center to form γ-keto alkoxide species, as the precursors to the aldol products. In contrast to these γ-keto alkoxide intermediates prevalent in condensation reactions, the alkoxides formed via C—C coupling between species derived from two carboxylic acids (Step 4, Scheme 5) retain the —OH group at the α-C-atom and the —COOH group at the γ-C-atom; dehydration of these groups can be catalyzed by a vicinal lattice O center to form β-keto carboxylates (Steps 5–7, Scheme 5), which then reprotonate to β-keto acids (Step 8, Scheme 5). These β-keto acid intermediates are very reactive and decarboxylate to form C$_3$ enolates (i.e. propen-2-olates) and CO$_2$ (Steps 9–11, Scheme 5). The propen-2-olate species subsequently reprotonate to form acetone, completing a ketonization turnover (Steps 12–13, Scheme 5). The lack of space velocity effects on rates (Section S10, SI) indicates that the adsorption constants (K_x^{-1}; Scheme 5) for H$_2$O (K_7^{-1}), CO$_2$ (K_{11}^{-1}), and acetone (K_{13}^{-1}) are very small and that the coverages of these species are thus kinetically-negligible on TiO$_2$(a) surfaces during ketonization catalysis.

Significant kinetic H/D isotope effects would indicate that bonds containing a H-atom form or cleave in kinetically-relevant steps. For instance, enolate formation, the kinetically-relevant step

in acetone condensation on TiO$_2$(a), gives a H/D isotope effect of 2.4 (523 K; Ref. [24]). The ketonization rates measured for ethanoic acid-d$_0$ and ethanoic acid-d$_4$ are, however, very similar ($r_H/r_D = 1.1 \pm 0.1$ at 0.6–2.2 kPa, TiO$_2$(a); Fig. 3a) and rule out the kinetic relevance of the α-C—H cleavage step that forms 1-hydroxy enolates from monodentate carboxylates (Step 3, Scheme 5). Such small observed H/D isotope effects would also be inconsistent with the kinetic relevance of any other step involving activation or cleavage of a C—H/O—H bond in Scheme 5 (i.e. Steps 5, 6, 8, 9, and 12). Thus, C—C coupling between 1-hydroxy enolates and coadsorbed AcO* (Step 4, Scheme 5) and decarboxylation of β-keto carboxylates (Step 10, Scheme 5) are the only plausible kinetically-relevant elementary steps consistent with measured H/D kinetic isotope effects.

The elementary steps in Scheme 5, taken together with (i) the pseudo-steady-state approximation for all bound species; (ii) the quasi-equilibrated nature of all steps except C—C coupling (Step 4, Scheme 5) and decarboxylation (Step 10, Scheme 5) steps; (iii) an irreversible decarboxylation step; and (iv) AcO* and * (bare Ti—O pairs) as the most abundant surface intermediates (MASI; from infrared spectra; Section 3.3) give the rate equation:

$$\frac{r}{[L]} = \frac{\overrightarrow{k_4}\overrightarrow{k_{10}}K_3K_1^2(P_{acid})^2}{\left(\dfrac{\overleftarrow{k_4}P_{H2O}}{\prod_{z=5}^{9}K_z} + \overrightarrow{k_{10}}\right)(1 + K_1P_{acid})^2} \qquad (6)$$

Here, $\overrightarrow{k_x}$, $\overleftarrow{k_x}$ and K_x are the respective forward and reverse rate constants and equilibrium constant for Step x in Scheme 5, and [L] is the number of catalytically relevant acid-base pairs on oxide surfaces (derivation in Section S11, SI). The weak effects of conversion and of H$_2$O pressure (0.02–0.2 kPa) on ketonization rates (Section S10, SI) indicate that the $\overleftarrow{k_4}P_{H2O}\left(\prod_{z=5}^{9}K_z\right)^{-1}$ term in Eq. (5) is much smaller than the $\overrightarrow{k_{10}}$ constant, which indicates, in turn, that the C—C coupling step (Step 4, Scheme 5) is irreversible and the sole kinetically-relevant step. Eq. (6) then becomes:
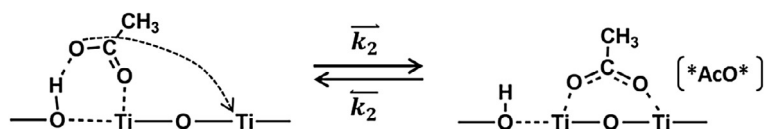
$$\frac{r}{[L]} = \frac{\overrightarrow{k_4}K_3K_1^2(P_{acid})^2}{(1 + K_1P_{acid})^2} \qquad (7)$$

The functional form of Eq. (7) accurately describes all rate data for ethanoic acid at 503–533 K (Fig. 3; regressed parameters shown in Tables 2 and 3) and leads to isotopic effects near unity for the

1. Dissociation of ethanoic acid on a Ti-O pair to form AcO*
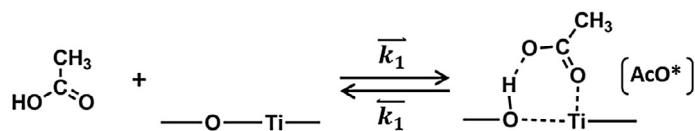
2. Dissociation of ethanoic acid on two Ti-O pairs to form *AcO*

3. α-C-H cleavage from AcO* to form 1-hydroxy enolate
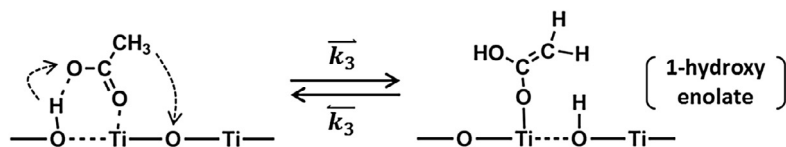
4. C-C coupling between 1-hydroxyl enolate and co-adsorbed AcO* to form α-hydroxy γ-carboxy alkoxide
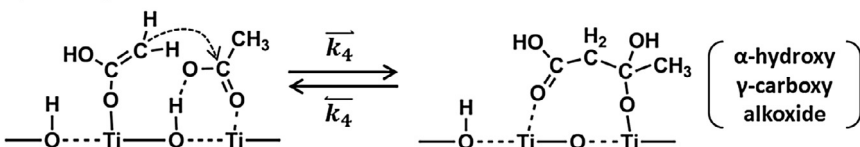
5. Dissociation of O-H bond in α-hydroxy γ-carboxy alkoxide to form γ-hydroxy γ-oxido carboxylate
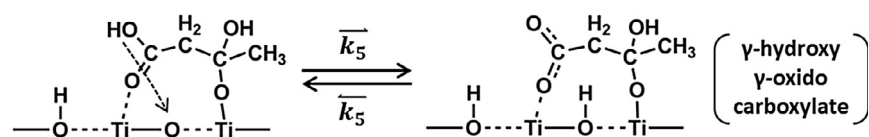
6. H_2O elimination from γ-hydroxy γ-oxido carboxylate to β-keto carboxylate
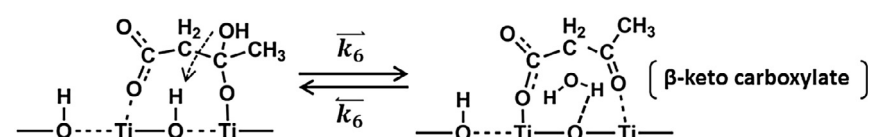
7. H_2O desorption
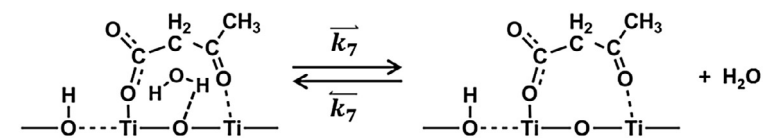
8. Protonation of β-keto carboxylate to form β-keto acid
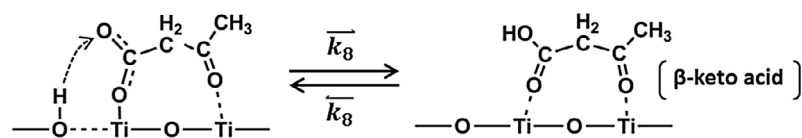
9. Dissociation of β-keto acid on a Ti-O-Ti structure
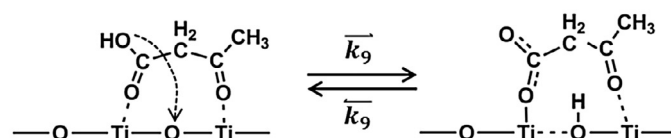
Scheme 5. Proposed elementary steps for carboxylic acid ketonization on acid-base pairs of TiO_2(a) (shown for ethanoic acid as an illustrative example).

10. Decarboxylation to form propen-2-olate
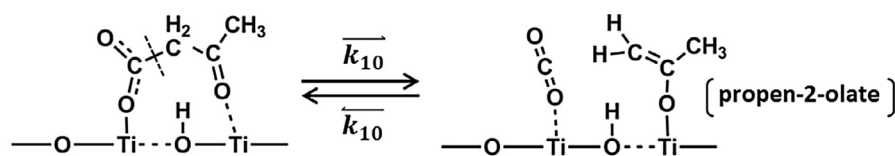
11. CO₂ desorption
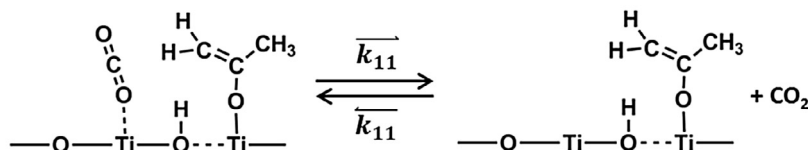
12. Protonation of propen-2-olate to acetone

13. Acetone desorption

Scheme 5 (*continued*)

$\vec{k}_4 K_3$ and K_1 terms in Eq. (7) (($(\vec{k}_4 K_3)_H / (\vec{k}_4 K_3)_D$ = 1.1, $(K_1)_H / (K_1)_D$ = 1.0, 523 K, Table 2), consistent with the kinetic relevance of the C—C coupling step (Step 4, Scheme 5) and with the involvement of H-atoms only in quasi-equilibrated steps, a conclusion confirmed by DFT treatments in Section 3.4, as also inferred above from the magnitude of the rates with perdeuterated and undeuterated reactants.
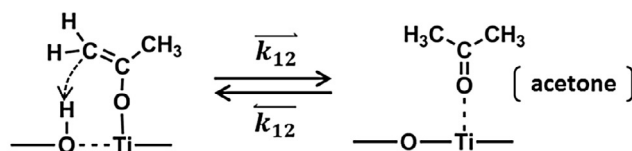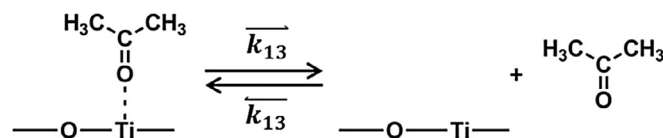
The K_1 term in Eq. (7) determines the fractional coverage (θ_{AcO^*}) of monodentate AcO* species bound at a Ti—O pair (θ_{AcO^*}; Step 1, Scheme 5):

$$\theta_{AcO^*} = \frac{K_1 P_{acid}}{1 + K_1 P_{acid}} \qquad (8)$$

The θ_{AcO^*} values range from 0.70 to 0.99 ML (523 K, 0.1–3.0 kPa ethanoic acid) when using K_1 values from ketonization rates and the functional form of Eq. (7) (24 ± 2 kPa⁻¹; Table 2). These values indicate that ketonization turnovers occur on TiO₂(a) surfaces

nearly saturated with AcO* species, a conclusion confirmed by *in-situ* infrared data (Section 3.3) and by DFT-derived adsorption energies (Section 3.4).

Ketonization rates of propanoic and butanoic acids are also described accurately by Eq. (7) (Fig. 3a). The regressed K_1 values for propanoic and butanoic acids (13 ± 2, 7.9 ± 0.6 kPa⁻¹; 523 K, Table 2) also lead to near saturation coverages (θ_{AcO^*} 0.56–0.97, propanoic acid; 0.44–0.96, butanoic acid; 523 K, 0.1–3.0 kPa acid). Thus, the kinetic relevance of the C—C coupling step (Step 4, Scheme 5) and the high coverages of monodentate carboxylates prevalent during catalysis seem to apply for the ketonization of C₂—C₄ carboxylic acids on TiO₂(a) surfaces.

Ketonization rates for ethanoic acid-d₀ and ethanoic acid-d₄ on rutile TiO₂ powders (TiO₂(r)) are also consistent with the functional form of Eq. (7) (Fig. 4; Table 2); these reactants give H/D iso-tope effects near unity for both $\vec{k}_4 K_3$ and K_1 (($(\vec{k}_4 K_3)_H / (\vec{k}_4 K_3)_D$ = 1.1, $(K_1)_H / (K_1)_D$ = 1.0, Table 2), indicative of similar pathways and active Ti—O pairs on TiO₂(r) and TiO₂(a). The regressed values of K_1 (5.4

Table 2
Regressed K_1, $\vec{k}_4 K_3$, ΔG_{AcO^*} and $\Delta G^{\ddagger}_{CC,a}$ values (to the functional form of Eq. (7)) for ketonization of C₂—C₄ carboxylic acids on TiO₂(a) and TiO₂(r) catalysts.[a]

Catalyst	Reactant	K_1[b] (kPa⁻¹)	ΔG_{AcO^*}[c] (kJ mol⁻¹)	$\vec{k}_4 K_3$[b] (10⁻⁶ (Ti-O)⁻¹ s⁻¹)	$\Delta G^{\ddagger}_{CC,a}$[d] (kJ mol⁻¹)
TiO₂(a)	CH₃COOH	24 ± 2	−33 ± 1	269 ± 3	166 ± 1
	CD₃COOD	24 ± 2	−33 ± 1	236 ± 4	167 ± 1
	C₂H₅COOH	13 ± 2	−30 ± 1	102 ± 3	170 ± 1
	C₃H₇COOH	7.9 ± 0.6	−28 ± 1	41 ± 1	175 ± 1
TiO₂(r)	CH₃COOH	5.4 ± 0.3	−27 ± 1	34 ± 1	175 ± 1
	CD₃COOD	5.4 ± 0.3	−27 ± 1	30 ± 1	176 ± 1

[a] 523 K; fitted data adopted from Fig. 3a for TiO₂(a) and Fig. 4 for TiO₂(r).
[b] Fitted using Eq. (7).
[c] Fitted using Eq. (9).
[d] Fitted using Eq. (13).

Table 3
Regressed K_1, $\vec{k_4}K_3$, ΔG_{AcO^*}, and $\Delta G_{CC,a}^{\ddagger}$ values (to the functional form of Eq. (7)) for ketonization of ethanoic acid on TiO_2(a) at temperatures between 503 K and 533 K and corresponding enthalpy and entropy components of free energies.[a]

T (K)	K_1^c (kPa^{-1})	$\Delta G_{AcO^*}^{\ d}$ (kJ mol^{-1})	ΔH_{AcO^*} (kJ mol^{-1})	ΔS_{AcO^*} (J mol^{-1} K^{-1})	$\vec{k_4}K_3^{\ c}$ (10^{-6} (Ti–O)$^{-1}$ s^{-1})	$\Delta G_{CC,a}^{\ddagger\ e}$ (kJ mol^{-1})	$\Delta H_{CC,a}^{\ddagger}$ (kJ mol^{-1})	$\Delta S_{CC,a}^{\ddagger}$ (J mol^{-1} K^{-1})
503	71 ± 7	−36 ± 1	−114 ± 3	−155 ± 6	77 ± 1	165 ± 1	137 ± 1	−56 ± 1
513	39 ± 4	−35 ± 1			145 ± 3	166 ± 1		
523[b]	24 ± 2	−33 ± 1			269 ± 3	166 ± 1		
533	15 ± 2	−32 ± 1			488 ± 7	167 ± 1		

[a] Fitted data adopted from Fig. 3b.
[b] Adopted from Table 2.
[c] Fitted using Eq. (7).
[d] Fitted using Eq. (9).
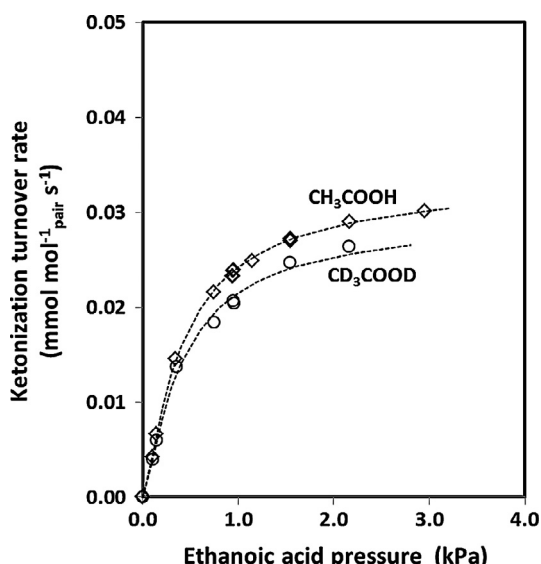[e] Fitted using Eq. (13).

Fig. 4. Effects of ethanoic acid pressure on ketonization turnover rates (ethanoic acid and ethanoic acid-d$_4$; TiO_2(r) + 20 wt.% Cu/SiO$_2$ (1:1 mass), 523 K, 20 kPa H$_2$ for undeuterated reactants, 20 kPa D$_2$ for deuterated reactants). Dashed lines represent the regressed fits to the mechanism-based functional form of Eq. (7).

vs. 24 kPa^{-1}) and $\vec{k_4}K_3$ (3.4×10^{-5} vs. 2.7×10^{-4} (Ti–O)$^{-1}$ s^{-1}) are, however, much smaller on TiO_2(r) than on TiO_2(a). Infrared spectra of TiO_2(r) during ketonization show that TiO_2(r) samples are covered with bidentate carboxylates bound at two vicinal Ti–O pairs (*AcO*; 0.2–1.6 kPa ethanoic acid, 523 K; Section 3.3), inconsistent with the high coverages of AcO* (θ_{AcO^*} 0.52–0.90; Eq. (8)) predicted from K_1 values regressed from rate data (5.4 ± 0.3 kPa^{-1}, Table 2). Such discrepancies indicate that ketonization does not take place on the majority low-index planes of TiO_2(r), the coverage on which is reflected in the infrared spectra, leading us to conclude, as in the case of aldol condensation of carbonyl compound on these materials [24], that it occurs instead on minority exposed planes of TiO_2(r) or on residual TiO_2(a) surfaces. This speculative hypothesis is confirmed by DFT-derived energies of ketonization elementary steps on TiO_2(r) (Section 3.4), which show a preference for *AcO* over AcO* species on TiO_2(r) surfaces and predict much lower ketonization rates on TiO_2(r) than on TiO_2(a).

The K_1 term in Eq. (7) reflects the free energy of carboxylic acid dissociation to form a monodentate carboxylate on a Ti–O pair (ΔG_{AcO^*}, Scheme 6):

$$K_1 = \exp(-\Delta G_{AcO^*}/RT) \tag{9}$$
$$\Delta G_{AcO^*} = G_{AcO^*} - G_{acid} - G_{Ti-O} \tag{10}$$

Here G_{AcO^*}, G_{acid}, and G_{Ti-O} are the free energies of the bound monodentate carboxylate (Step 1, Scheme 5), the gaseous carboxylic acid, and the Ti–O pair. The $\vec{k_4}K_3K_1^2$ numerator term in Eq. (7) reflects, in turn, the free energy difference between the C–C coupling TS ($G_{CC}^{\ddagger}$; Step 4, Scheme 5) and two gaseous acid reactants and two bare Ti–O pairs ($\Delta G_{CC}^{\ddagger}$, Scheme 6):

$$\vec{k_4}K_3K_1^2 = \frac{k_B T}{h}\exp(-\Delta G_{CC}^{\ddagger}/RT) \tag{11}$$
$$\Delta G_{CC}^{\ddagger} = G_{CC}^{\ddagger} - 2G_{acid} - 2G_{Ti-O} \tag{12}$$

The $\vec{k_4}K_3$ term, determined from measured $\vec{k_4}K_3K_1^2$ (Eq. (11)) and K_1 (Eq. (9)) values, represents the maximum ketonization turnover rate (r_{max}); it is achieved as monodentate AcO* species reach saturation coverages:

$$r_{max} = \vec{k_4}K_3 = \frac{k_B T}{h}\exp\left(-\Delta G_{CC,a}^{\ddagger}/RT\right) \tag{13}$$

Here $\Delta G_{CC,a}^{\ddagger}$ represents the free energy of the C–C coupling TS (Step 4) with respect to two bound AcO* species on TiO_2(a) surfaces (Scheme 6):

$$\Delta G_{CC,a}^{\ddagger} = G_{CC}^{\ddagger} - 2G_{AcO^*} \tag{14}$$

Table 2 reports ΔG_{AcO^*} and $\Delta G_{CC,a}^{\ddagger}$ values from the K_1 and $\vec{k_4}K_3$ parameters from all rate data regressed to the functional form of Eq. (6) for C$_2$–C$_4$ carboxylic acids on TiO_2(a). The ΔG_{AcO^*} values (523 K; Table 2) become less negative as the alkyl chain in the carboxylic acid lengthens (−33 ± 1 kJ mol^{-1}, ethanoic acid; −28 ± 1 kJ mol^{-1}, butanoic acid), indicative of steric effects that weaken AcO* binding at the nearly saturated TiO_2(a) surfaces present during ketonization catalysis.

$\Delta G_{CC,a}^{\ddagger}$ values (523 K; Table 2) became more positive with increasing alkyl chain length (166 ± 1 kJ mol^{-1}, ethanoic acid; 175 ± 1 kJ mol^{-1}, butanoic acid). These trends reflect, in part, the stronger steric hindrance imposed by the larger alkyl groups in the 1-hydroxy enolate and coadsorbed AcO* components of the C–C coupling TS than for its two AcO* precursors (Step 4, Scheme 5); they also arise, to some extent, from electron-donating alkyl substituents that make the α-C-atom in 1-hydroxy enolate a weaker nucleophile [51]. Alkyl substituents have the opposite effects on the decarboxylation of β-keto carboxylates (Step 10, Scheme 5) than on the C–C coupling step. Stronger repulsion between the larger alkyl groups at the α-C and β-C positions of β-keto carboxylates favors CO$_2$ elimination. The alkyl group at the α-C position also stabilizes the decarboxylation TS via p-π conjugation with the incipiently formed C=C bond. The consequent higher decarboxylation rates as alkyl chains lengthen provide additional evidence for the kinetic irrelevance of this step, because measured $\Delta G_{CC,a}^{\ddagger}$ values increase with increasing alkyl substitution (Table 2).
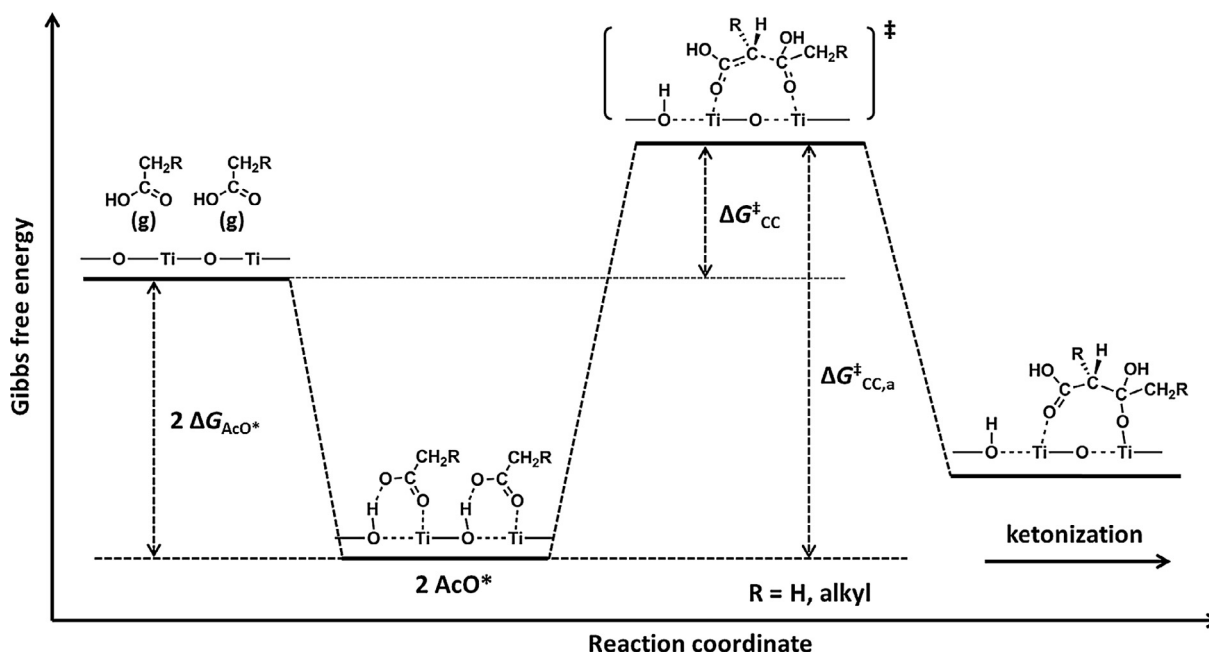
Scheme 6. Schematic reaction coordinate diagram for carboxylic acid ketonization on TiO$_2$(a).

The enthalpy and entropy components of measured ΔG_{AcO^*} and $\Delta G^{\ddagger}_{CC,a}$ values for ethanoic acid were obtained by regressing the rate and equilibrium constants in Eq. (7) from rate data at different temperatures (503–533 K; $\Delta G = \Delta H - T\Delta S$; Table 3). The ΔH_{AcO^*} and ΔS_{AcO^*} values for the adsorption of ethanoic acid as monodentate carboxylates on TiO$_2$(a) are -114 ± 3 kJ mol^{-1} and -155 ± 6 J mol^{-1} K^{-1}, respectively (Table 3), reflecting the predominant enthalpic component in ΔG_{AcO^*} values at these temperatures. Measured $\Delta H^{\ddagger}_{CC,a}$ and $\Delta S^{\ddagger}_{CC,a}$ values for ethanoic acid ketonization on TiO$_2$(a) are 137 ± 1 kJ mol^{-1} and -56 ± 1 J mol^{-1} K^{-1} (Table 3). These enthalpy and entropy values, taken together with the respective free energies, allow accurate benchmarking of experimental and theoretical methods in determining the preferred ketonization pathways and the kinetic relevance of the steps and intermediates that mediate ketonization turnovers on TiO$_2$(a) surfaces (Section 3.4).

The evidence presented above indicates that ketonization of C$_2$–C$_4$ carboxylic acids proceeds via kinetically-relevant C–C coupling transition states on Ti–O pairs of TiO$_2$(a) surfaces essentially saturated with monodentate carboxylates bound at acid-base pairs. These conclusions are confirmed below by the infrared detection of the adsorbed species prevalent during ketonization catalysis (Section 3.3) and by theoretical assessments of the stability of adsorbed species and transition states over a broad range of surface coverages (1/8–1 ML) (Section 3.4).

3.3. Infrared study of adsorbed species derived from ethanoic acid adsorption on anatase and rutile TiO$_2$ at catalytic temperatures

Infrared spectra were collected during ethanoic acid ketonization on TiO$_2$(a) and TiO$_2$(r) at 523 K and 0.2–1.6 kPa ethanoic acid in order to assess the type, coverage, and kinetic involvement of adsorbed species. Ethanoic acid (AcOH) can dissociate to form monodentate (AcO*; Step 1, Scheme 5) or bidentate (*AcO*; Step 2, Scheme 5) carboxylates at one or two Ti–O pairs; it can also bind molecularly via H-bonding at a Ti–O pair (AcOH*) [3]. DFT-derived binding energies show that the relative coverages of AcO* and AcOH* depend on the strength of the basic lattice O-atom (Section 3.4). AcO* is much more stable than AcOH* on Ti–O pairs in TiO$_2$(a); in contrast, AcOH* is the most stable monodentate form
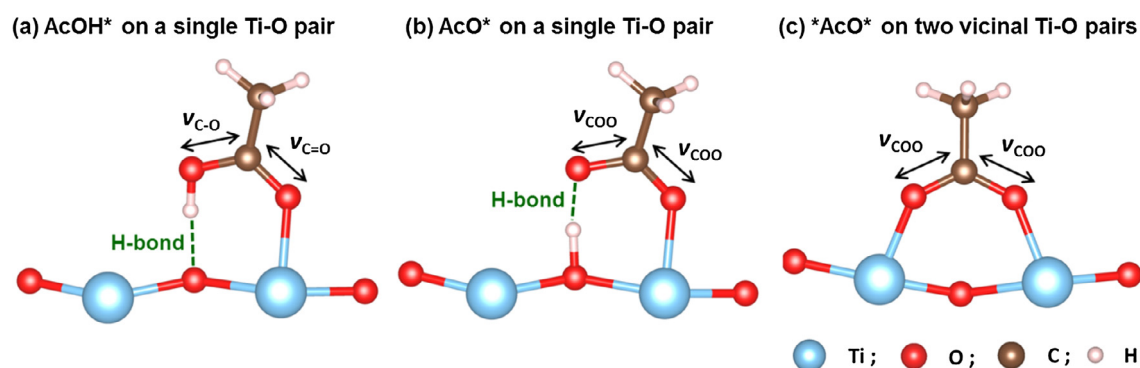
on TiO$_2$(r), because its coordinatively-unsaturated O-atoms are more weakly basic than those on TiO$_2$(a) (E_{PA} −1097 vs. −1175; Section 3.4). These carboxylate and molecular forms can be distinguished by stretching modes of their respective carboxyl or carboxylate moieties (—C(=O)OH, —C(=O)O—). AcOH* binds with its O-atom at the Ti center of a Ti–O pair and its hydroxy H-atom at the O-atom of this Ti–O pair (Scheme 7a). AcO* species binds in monodentate form with its two O-atoms at the Ti center of a Ti–O pair and at the abstracted H-atom, which is bound at the O-atom in the Ti–O pair (Scheme 7b). In contrast, *AcO* species binds in bidentate form with each of its two O-atoms at one Ti center in two vicinal Ti–O pairs (Scheme 7c).

DFT-derived vibrational frequencies for these modes were used to assign these bands and to determine the relative stability of these species as a function of coverage on TiO$_2$ surfaces. Surface coverages (θ_{acid}) are defined here based on Ti–O pairs:

$$\theta_{acid} = \frac{n_{acid}}{n_{Ti-O}} \tag{15}$$

where n_{acid} is the number of adsorbed carboxylic acid molecules and n_{Ti-O} is the number of exposed Ti–O pairs. The maximum θ_{acid} value for each form is set by their respective binding stoichiometries (1 for AcOH* and AcO*, 1/2 for *AcO*). DFT-derived frequencies for C=O and C–O stretches of AcOH* on TiO$_2$(a) are 1641–1659 cm^{-1} and 1480–1493 cm^{-1}, respectively (at 1/6–1 ML; Table 4). The antisymmetric ν_{COO} ($\nu_{COO,as}$) and symmetric ν_{COO} ($\nu_{COO,s}$) vibrations in AcO* on TiO$_2$(a) appear at 1540–1564 cm^{-1} and 1379–1409 cm^{-1}, respectively (at 1/6–1 ML; Table 4); these frequencies are at 1529–1531 cm^{-1} ($\nu_{COO,as}$) and 1435–1437 cm^{-1} ($\nu_{COO,s}$) for *AcO* (at 1/8–1/2 ML; Table 4).

The infrared spectra on TiO$_2$(a) after treatments of He at 573 K for 2 h exhibit O–H bands (3667 cm^{-1}; Fig. 5a), assigned to titanol species at surface defects ubiquitous on oxide crystallites [52,53]. Contact with ethanoic acid (1.0 kPa) at 523 K caused these O–H bands on TiO$_2$(a) surfaces to shift to lower wavenumbers and to merge with a broader and more intense band centered at 3150 cm^{-1}, which is assigned to OH species derived from the dissociation of ethanoic acid to form either AcO* or *AcO* (Schemes 7b and c); such a frequency shift relative to isolated

(a) AcOH* on a single Ti-O pair   **(b) AcO* on a single Ti-O pair**   **(c) *AcO* on two vicinal Ti-O pairs**

Scheme 7. DFT-derived adsorption modes for ethanoic acid on Ti—O pairs (PBE + D3BJ, PAW, TiO_2(a) (1 0 1) surfaces).

Table 4
DFT-derived frequencies for AcOH*, AcO*, and *AcO* on TiO_2 surfaces.[a]

Oxide	Mode	θ_{acid} range (ML)	Frequency (cm^{-1})		
TiO_2(a)			$v_{C=O}$	v_{C-O}	v_{CH3}
	AcOH*	1/6–1	1641–1659	1480–1493	2985–2991
			$v_{COO,as}$	$v_{COO,s}$	v_{CH3}
	AcO*	1/6–1	1540–1564	1379–1409	2982–2990
	AcO	1/8–1/2	1529–1531	1435–1437	2988–2990
TiO_2(r) [b]			$v_{C=O}$	v_{C-O}	v_{CH3}
	AcOH*	1/4–1	1584–1604	1473–1485	2989–2997
			$v_{COO,as}$	$v_{COO,s}$	v_{CH3}
	AcO	1/8–1/2	1514–1522	1432–1444	2989–2993

[a] PBE + D3BJ, PAW, using TiO_2(a) (1 0 1) and TiO_2(r) (1 1 0) surfaces as the respective models; computational details described in Section 2.4.
[b] No stable AcO* structures can be isolated during energy and geometry optimizations because of the weakly basic nature of the O-atoms on TiO_2(r) surfaces.

Ti—OH species reflects the effects of H-bonding [22] at the prevalent dense adlayers. These isolated titanols are present as minority species and are thus not explicitly considered as active structures in the DFT treatments of ketonization elementary steps (Section 3.4).

Three distinct bands appeared upon contact of TiO_2(a) with ethanoic acid at 523 K (2936, 1548, and 1385 cm^{-1}) together with those for the gaseous reactants (3596, 3581, 3566, 1796, 1776 cm^{-1}) [53] and the CO_2(g) ketonization product (2362 cm^{-1}) [54]. DFT treatments show that the bands at 1548 and 1385 cm^{-1} correspond to $v_{COO,as}$ and $v_{COO,s}$ vibrations in AcO*, respectively (DFT: 1540–1564 cm^{-1}, 1379–1409 cm^{-1}; Table 4). The band at 2936 cm^{-1} corresponds to the —CH_3 stretch (v_{CH3}) in AcO* (DFT: 2982–2990 cm^{-1}; Table 4) [55]. The frequencies of these $v_{COO,as}$ and $v_{COO,s}$ bands were essentially unperturbed by changes in ethanoic acid pressure (0.2–1.6 kPa; Fig. 6a), indicating that AcO* is the predominant carboxylate and that it is present at near-saturation coverages on TiO_2(a) at all conditions. The intensity of the —CH_3 stretch band increased with increasing ethanoic acid pressure in a Langmuir manner (Fig. 6a; Eq. (8)) with a K_1 value (24 ± 3 kPa^{-1}, Fig. 6a) that is similar to that derived from ketonization rate data and Eq. (6) (24 ± 2 kPa^{-1}, Table 2; Fig. 3a). These K_1 values show that monodentate carboxylates (AcO*) are present at high coverages (θ_{AcO^*} 0.83–0.97 ML) as the predominant adsorbed species on TiO_2(a) at all conditions of relevant ketonization catalysis.

The removal of ethanoic acid from the contacting gas phase led to the gradual disappearance of the bands for AcO* and CO_2(g) on TiO_2(a) samples (Fig. 5a) over 2 h at 523 K and to the concurrent appearance of bands at 1538 and 1428 cm^{-1} (Fig. 5a); these bands correspond to $v_{COO,as}$ and $v_{COO,s}$ stretches in bidentate carboxylates (*AcO*) according to DFT estimates (1529–1531 cm^{-1}, 1435–1437 cm^{-1}; Table 4). The intensity of these *AcO* bands decreased very gradually with time and the bands became undetectable after

treatment in He at 523 K for 26 h. These treatments in He at 523 K also led to the full recovery of initial ketonization rates on TiO_2(a) samples deactivated (for 22 h to 0.76 of initial rates; 523 K, 1.0 kPa ethanoic acids; Section 3.1). The recombinative desorption of the active AcO* species leads to a decrease in their coverage with time; the concomitant increase in vacant sites (*) then allow the gradual formation of *AcO* as the stable form of adsorbed ethanoic acid on TiO_2(a) surfaces. The slow removal of these *AcO* species in an inert environment is consistent with the nature of the regeneration treatments that led to the recovery of initial ketonization rates on deactivated samples and also with the proposal that bidentate carboxylates act as unreactive spectator species that prevent access to the Ti—O pairs required for ketonization turnovers.

Exposure of TiO_2(r) to gaseous ethanoic acid (1.0 kPa, 523 K; Fig. 5b) led to bands similar to those observed on TiO_2(a), but at lower frequencies (1522, 1401 cm^{-1}). These bands correspond to $v_{COO,as}$ and $v_{COO,s}$ stretches in bidentate carboxylates (*AcO*), an assignment based on DFT-derived frequencies (1514–1522 cm^{-1}, 1432–1444 cm^{-1}, Table 4) and on spectroscopic and theoretical evidence for the prevalence of *AcO* over AcOH* and AcO* on TiO_2(r) [3,52]. These $v_{COO,as}$ and $v_{COO,s}$ frequencies did not change with ethanoic acid pressure (0.2–1.6 kPa; Fig. 6b) or after removal of ethanoic acid from contact with the catalysts for 0.5 h (Section S12, SI); thus, we conclude that bidentate carboxylates (*AcO*) are the MASI on TiO_2(r) during ketonization catalysis, in distinct contrast to the prevalence of monodentate AcO* species on TiO_2(a) surfaces. The integrated intensity of the v_{CH3} band (2932 cm^{-1}) on TiO_2(r) was unaffected by the ethanoic acid pressure (0.2–1.6 kPa; Fig. 6b), indicative of the presence of *AcO* species at near saturation coverages. The regressed fits of these coverages on TiO(r) to the Langmuir form of Eq. (8) give a K_1 value of 190 ± 3 kPa^{-1} (Fig. 6b), a value that differs markedly from that derived from the rate data and Eq. (7) on TiO_2(r) (5.4 ± 0.3 kPa^{-1}, Table 2; Fig. 4). Thus, the species detected in the infrared spectra on TiO_2(r) sur-
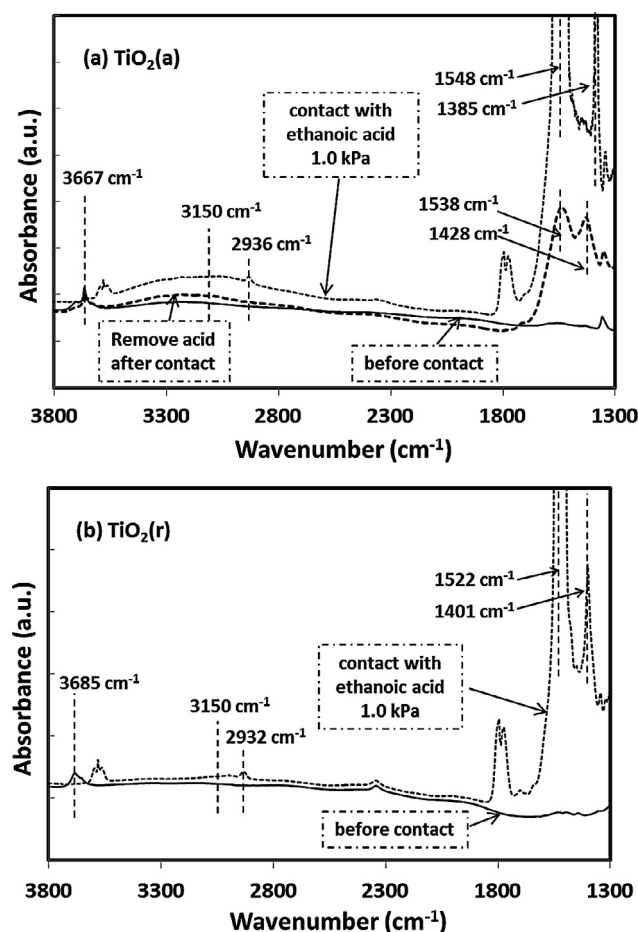
Fig. 5. IR spectra of (a) TiO$_2$(a) and (b) TiO$_2$(r) with 1.0 kPa ethanoic acid during steady-state ketonization at 523 K (spectra before and after the acid contact shown as reference).

Fig. 6. Frequencies for $\nu_{COO,as}$ and $\nu_{COO,s}$ bands and the integrated intensity of the infrared bands for adsorbed ethanoic acid (2960–2900 cm^{-1}) on (a) TiO$_2$(a) and (b) TiO$_2$(r) as a function of ethanoic acid pressure (523 K). The integrated intensities were normalized by their maximum values (1.6 kPa). Solid lines indicate qualitative trends. Dashed curves represent the regressed fits to the functional form of Eq. (8) with the regressed parameter K_1 shown in parenthesis.

faces differ from those that account for the denominator term in Eq. (7). These different K_1 values can only be reconciled by considering the carboxylate species that occupy the Ti—O pairs responsible for catalytic turnovers to be present only as minority species, with the bidentate carboxylates prevalent in the infrared spectra as the majority species but without their detectable catalytic involvement.

We conclude based on this evidence that ketonization reactivity reflects such minority sites and that they are likely to reflect the presence of anatase-like structures in these TiO$_2$(r) samples. Ultraviolet Raman spectra have shown that the phase transformation from anatase to rutile TiO$_2$ requires a higher temperature at the surface than in the bulk crystal (973 vs. 823 K) [56], indicating that anatase-like structures may be retained at the surface of some of the crystallites present in TiO$_2$(r) samples even after the bulk of most crystals has converted to the rutile structure. These conclusions are consistent with the lower turnover rates observed on TiO$_2$(r) compared with TiO$_2$(a) and with DFT-derived energetics that would lead to areal ketonization rates on TiO$_2$(r) (110) surfaces even lower than those measured on TiO$_2$(r) powders (Section 3.4).

These spectra and their theoretical analysis indicate that monodentate AcO* species predominate on TiO$_2$(a) and act as reactive intermediates in ketonization turnovers. Bidentate *AcO* species prevail on TiO$_2$(r) but are not involved in ketonization turnovers. These data and conclusions contradict the previously proposed involvement of bidentate carboxylates (*AcO*) as reactive intermediates in ketonization turnovers on TiO$_2$ and ZrO$_2$ surfaces [14,16–
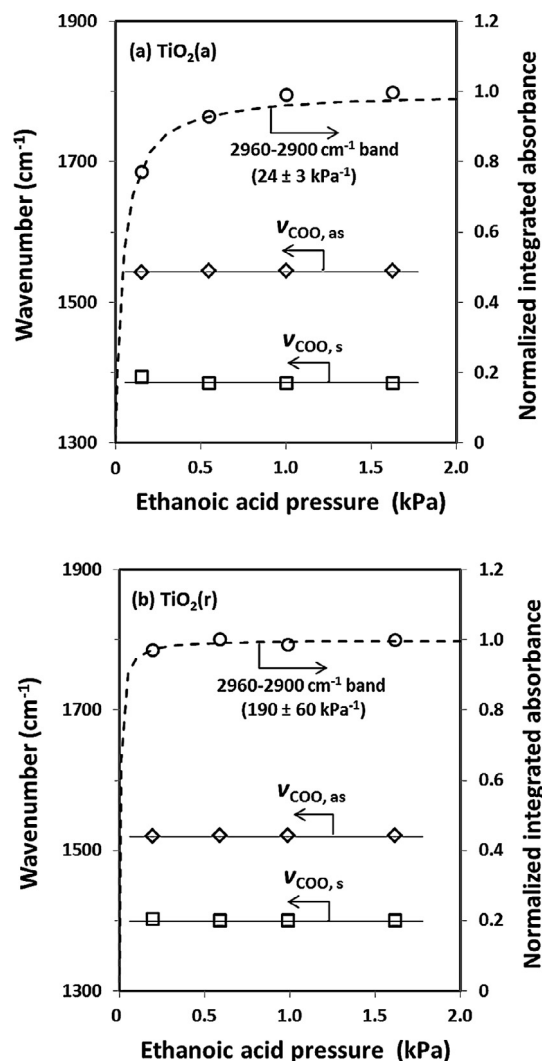
21]. These unreactive bidentate species desorb slowly as gaseous ketene molecules; their scavenging by hydrogenation on Cu sites accounts for both the formation of ethanal and ethanol and for the inhibition of deactivation brought forth by the presence of gaseous H$_2$ and a Cu function during ketonization of ethanoic acid on TiO$_2$ and ZrO$_2$ (Section 3.1).

3.4. Theoretical assessment of ketonization elementary steps and adsorbed species on anatase and rutile TiO$_2$ surfaces

TiO$_2$(a) and TiO$_2$(r) surfaces preferentially expose their most stable (101) and (110) planes, respectively [40]. These surface planes are used here as periodic slab models in DFT estimates of the binding and reactive properties of Ti—O pairs. We address the involvement of Ti—O pairs in the stabilization of adsorbed species and transition states involved in the elementary steps that mediate ethanoic acid ketonization turnovers (Scheme 5). In doing so, we also assess the influence of the strength of the acid and base sites and the Ti—O distances on adsorption and activation free energies.
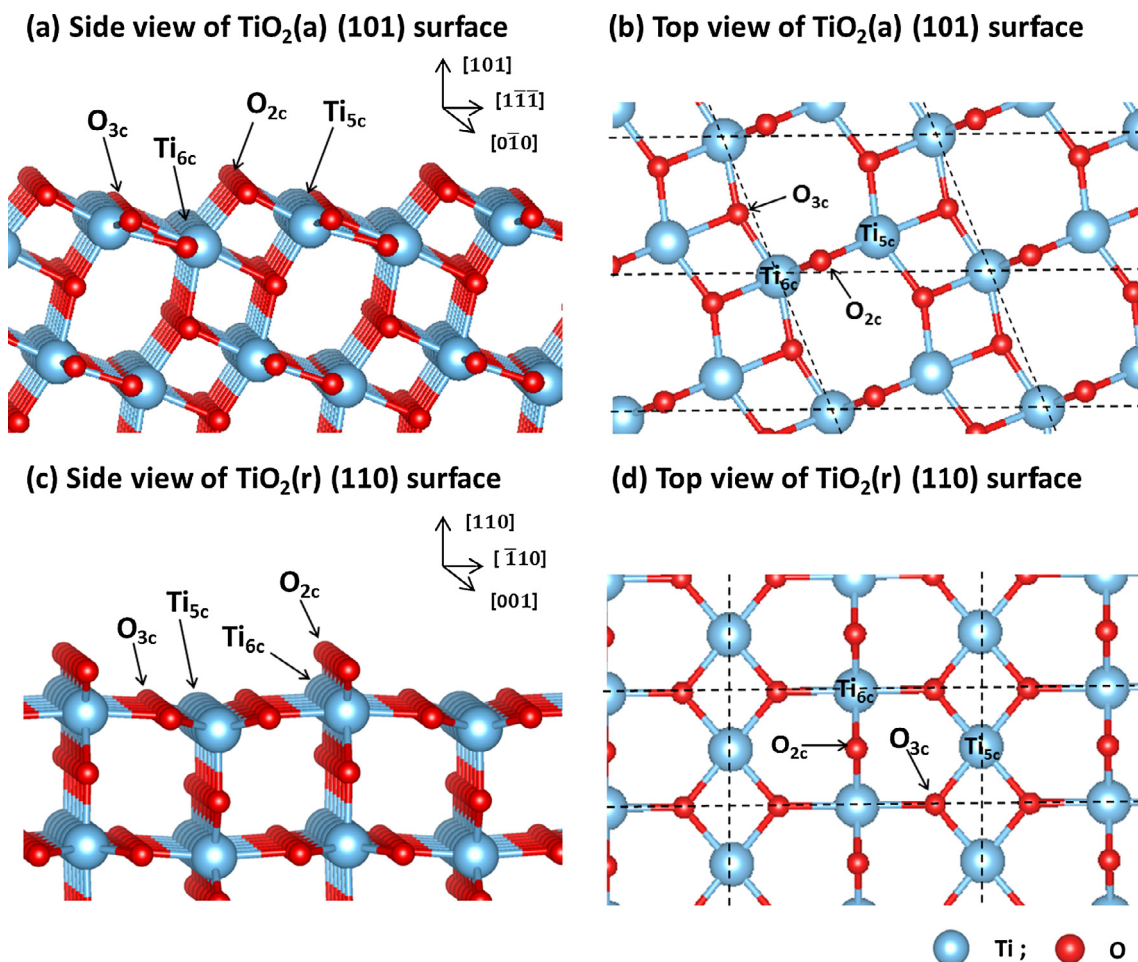
TiO$_2$(a) (101) surfaces exhibit sawtooth-like corrugations that expose two types of Ti cations and two types of O anions (Scheme 8a and b) [22]. One of the Ti centers exhibits sixfold coordinative saturation, as the Ti atoms do in the anatase bulk (Ti$_{6c}$, coordination number (CN) of 6), while the other Ti center is five-coordinate and is coordinatively-unsaturated (Ti$_{5c}$, CN 5). Their connecting O-atoms have either twofold (O$_{2c}$, CN 2) or threefold (O$_{3c}$, CN 3) coordination.

The affinity of a gaseous OH$^-$ anion (E_{HA}; Eq. (3)) can be used to assess the acid strength of these two types of Ti Lewis centers. The affinity of a gaseous proton (E_{PA}; Eq. (4)) can be used, in turn, to assess the strength of the basic O-anions. These OH$^-$ and H$^+$ affinities are more negative on Ti and O centers with lower coordination numbers (Table 5), as expected from their coordinative unsaturation, which allows effective orbital overlap with adsorbed molecules. In fact, the OH$^-$ affinity of coordinatively-saturated Ti$_{6c}$ centers (E_{HA}(Ti$_{6c}$)) is nearly zero (<−1 kJ mol^{-1}, Table 5); they cannot bind intermediates and transition states, thus rendering Ti$_{6c}$ sites inactive in ketonization catalysis, as also concluded in the case of condensation reactions on TiO$_2$(a) surfaces [24]. We surmise, and then show below, that Ti$_{5c}$ sites (E_{HA} −246 kJ mol^{-1}, Table 5) are the only Ti centers able to stabilize adsorbed acid molecules and the transition states that mediate their reactions; therefore, they are the Ti centers in the Ti—O pairs responsible for ketonization turnovers on TiO$_2$(a) (101) surfaces. In contrast, the E_{PA} values for the O$_{2c}$ and O$_{3c}$ sites are both significant in magnitude and differ by 37 kJ mol^{-1} (−1175 vs. −1138 kJ mol^{-1},

Table 5), suggesting that both basic sites can interact with the acidic proton at the OH group in the acid reactants.

TiO$_2$(r) (110) surfaces also expose Ti$_{5c}$, Ti$_{6c}$, O$_{2c}$, and O$_{3c}$ ions (Scheme 8c and d) but with very different connectivity than on TiO$_2$(a) (101), as expected from the different crystal symmetry of these two TiO$_2$ phases (TiO$_2$(r): tetragonal, P4$_2$/mnm; TiO$_2$(a): tetragonal, I4$_1$/amd) [40]. The coordinatively-unsaturated Ti$_{5c}$ sites on TiO$_2$(r) (110) are linked by O$_{3c}$ atoms and do not exhibit direct bonding with any O$_{2c}$ atoms (Table 5). Such surface arrangements lead to shorter distances between two neighboring Ti$_{5c}$ sites ($d_{Ti5c–Ti5c}$ = 0.299 nm) but longer Ti$_{5c}$—O$_{2c}$ distances ($d_{Ti5c–O2c}$ = 0.360 nm) than on TiO$_2$(a) (101) surfaces (0.383 nm, 0.184 nm, Table 5). Also, the E_{HA}(Ti$_{5c}$) values on TiO$_2$(r) (110) surfaces are much more negative than on TiO$_2$(a) (101) surfaces (−369 vs. −246 kJ mol^{-1}, Table 5), indicative of much stronger Lewis acid centers. In contrast, the E_{PA}(O$_{2c}$) and E_{PA}(O$_{3c}$) values are less negative on TiO$_2$(r) (110) (−1093 kJ mol^{-1}, −1008 kJ mol^{-1}, Table 5) than on TiO$_2$(a) (101) surfaces (−1175 kJ mol^{-1}, −1138 kJ mol^{-1}, Table 5), indicating that O-atoms are less basic on TiO$_2$(r). Not unexpectedly, these differences in Ti—O distances and acid-base strength lead to very different binding modes and reactivity of adsorbed acid molecules on TiO$_2$(a) and TiO$_2$(r), as discussed in detail below.

Ethanoic acid can form molecular AcOH* or dissociated AcO* at Ti$_{5c}$—O$_{2c/3c}$ pairs on TiO$_2$(a) (101) surfaces. Their relative abundance depends on the basicity of the accessible lattice O-atoms that must interact with the —OH group in ethanoic acid. The

(a) Side view of TiO$_2$(a) (101) surface

(b) Top view of TiO$_2$(a) (101) surface

(c) Side view of TiO$_2$(r) (110) surface

(d) Top view of TiO$_2$(r) (110) surface

Ti ;   O

Scheme 8. Structures of TiO$_2$(a) (101) and TiO$_2$(r) (110) surfaces.

Table 5
DFT-derived hydroxide anion affinities (E_{HA}), proton affinities (E_{PA}), and the shortest distances between two Ti_{5c} sites ($d_{Ti5c\text{-}Ti5c}$) and between one Ti_{5c} site and one O_{2c} site ($d_{Ti5c\text{-}O2c}$) on $TiO_2(a)\,(1\,0\,1)$ and $TiO_2(r)\,(1\,1\,0)$ surfaces.[a]

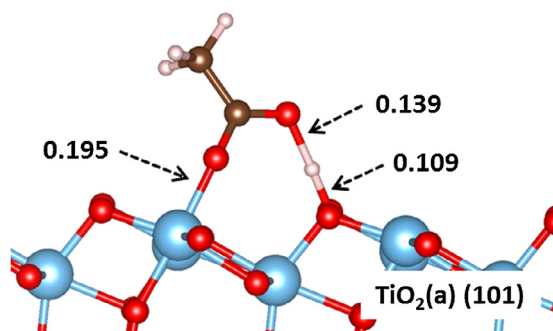| Surface	E_{HA} (kJ mol^{-1})		E_{PA} (kJ mol^{-1})		$d_{Ti5c\text{-}Ti5c}$ (nm)	$d_{Ti5c\text{-}O2c}$ (nm)
	Ti_{5c}	Ti_{6c}	O_{2c}	O_{3c}		
$TiO_2(a)\,(1\,0\,1)$	−246	<−1	−1175	−1138	0.383	0.184
$TiO_2(r)\,(1\,1\,0)$	−369	<−1	−1093	−1008	0.299	0.360

[a] PBE + D3BJ, PAW.

weaker O_{3c} site preserves the O—H bond intact upon adsorption (O—H distance: 0.105 nm vs. 0.099 nm in AcOH (g), Scheme 9a) and forms weakly-adsorbed AcOH* species at Ti_{5c}–O_{3c} pairs. The O—H bond in AcOH is cleaved to form AcO* (O—H distance: 0.139–0.143 nm, Scheme 9b and c) at Ti_{5c}–O_{2c} pairs consisting of Ti_{5c} centers with O_{2c} sites at either the first or second coordination shell (Ti_{5c}–O_{2c} distance: 0.184 vs. 0.413 nm, Scheme 9b and c); this is also evident from the nearly-formed H—O_{2c} bond on both

(a) AcOH* on a Ti$_{5c}$-O$_{3c}$ pair

0.105, 0.218, 0.154

TiO$_2$(a) (101)

(b) AcO* on a bonded Ti$_{5c}$-O$_{2c}$ pair

0.143, 0.108, 0.198
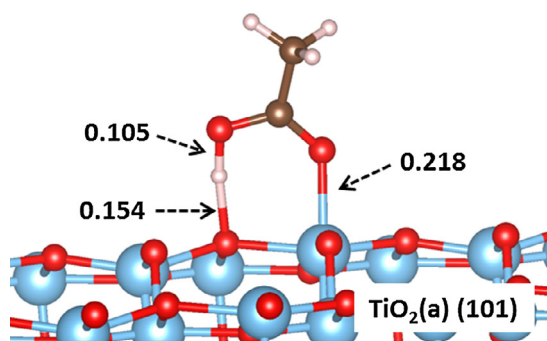
TiO$_2$(a) (101)

(c) AcO* on a unbounded Ti$_{5c}$-O$_{2c}$ pair

0.195, 0.139, 0.109

TiO$_2$(a) (101)

(d) *AcO* on two Ti$_{5c}$-O$_{2c}$ pairs

0.207, 0.099, 0.231, 0.210

TiO$_2$(a) (101)

(e) AcOH* on a Ti$_{5c}$-O$_{2c}$ pair

0.211, 0.108, 0.142

TiO$_2$(r) (110)

(f) *AcO* on two Ti$_{5c}$-O$_{2c}$ pairs

0.208, 0.230, 0.211

TiO$_2$(r) (110)

Ti ; O ; C ; H
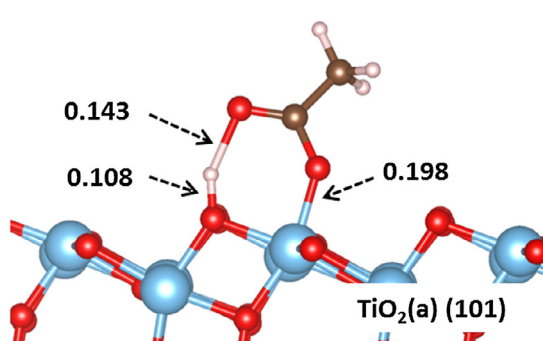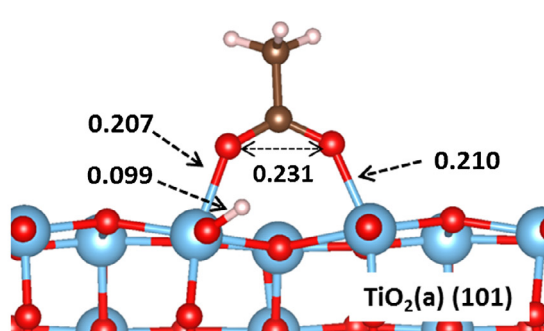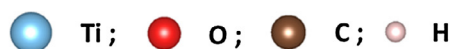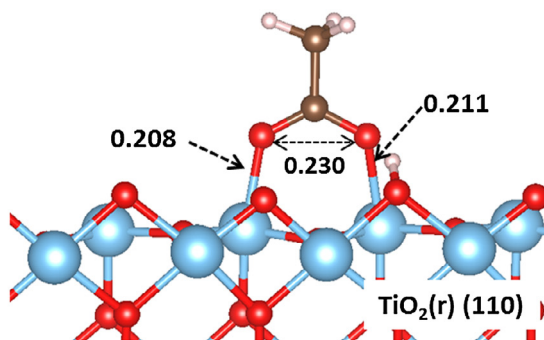
Scheme 9. DFT-derived adsorption modes for ethanoic acid on $TiO_2(a)\,(1\,0\,1)$ and $TiO_2(r)\,(1\,1\,0)$ surfaces (PBE + D3BJ, PAW, θ_{acid} = 1/2 ML). Only one acid molecule is shown on the surface for clarity; distances are given in nm.

Ti_{5c}—O_{2c} structures (H—O_{2c} distance: 0.108–0.109 vs. 0.099 nm in products, Scheme 9b and c). DFT-derived adsorption free energies (ΔG_{ads}; 1/2 ML, 523 K, 1 bar) for the AcO* modes at these two Ti_{5c}—O_{2c} structures were nearly identical (−52 and −51 kJ mol⁻¹; Section S13, SI) and much more negative than for AcOH* at the Ti_{5c}—O_{3c} pair (−15 kJ mol⁻¹; Section S13, SI), thus making AcO* species the predominant monodentate form of adsorbed ethanoic acid on $TiO_2(a)$. The most stable *AcO* structure on $TiO_2(a)$ (1 0 1) surfaces is also located at Ti_{5c}—O_{2c} pairs, with the two carboxylate O-atoms each bound to one of two neighboring Ti_{5c} centers and the dissociated H-atom coordinated to the basic O_{2c} site (Scheme 9d). These stronger acid-base Ti_{5c}—O_{2c} pairs are used in the DFT treatments of ketonization elementary steps that are described next.

The DFT-derived ΔG_{ads} values for AcO* species bound at Ti_{5c}—O_{2c} pairs on $TiO_2(a)$ (1 0 1) surfaces vary from −55 to −50 kJ mol⁻¹ (525 K, 1 bar; Eq. (2)) as the acid coverage (θ_{acid}) increases (1/6–1 ML, Fig. 7a); the respective adsorption enthalpies (ΔH_{ads}) vary from −132 to −140 kJ mol⁻¹ (Fig. 7b). These small differences in ΔG_{ads} and ΔH_{ads} values indicate that the distances between Ti_{5c} centers at $TiO_2(a)$ (1 0 1) surfaces ($d_{Ti5c-Ti5c}$ 0.383 nm, Table 5) do not lead to strong lateral repulsion among AcO* species, even at the saturation coverages prevalent during ketonization catalysis.

In contrast, DFT-derived ΔG_{ads} values for bound *AcO* species at these Ti_{5c}—O_{2c} pairs become much less negative (−82 to −43 kJ mol⁻¹) with increasing acid coverage (1/8 to saturation 1/2 ML) (Fig. 7a). Such destabilization predominantly reflects the ΔH_{ads} component in ΔG_{ads} (Fig. 7b). Similarly, the Ti_{5c}—Ti_{5c} distances in $TiO_2(a)$ (1 0 1) preclude repulsive interactions among alkyl groups in vicinal *AcO* species, as in the case of AcO* above. These Ti_{5c}—Ti_{5c} distances at the two vicinal Ti_{5c} centers linked to the O atoms in the bound *AcO* (Scheme 9d) increase slightly from 0.381 nm to 0.384 nm as acid coverage increases (1/8 to saturation 1/2 ML), while the O—O distances in *AcO* remain nearly unchanged (d_{O-O} 0.231–0.232 nm, Scheme 9d). These changes with coverage lead to somewhat less effective overlap between Ti and O orbitals in *AcO* and to the concomitant *AcO* destabilization as coverage increases (Fig. 7a).

The above effects of acid coverage on ΔG_{ads} values for AcO* and *AcO* species (Fig. 7a) indicate that *AcO* species dominate at acid coverages below 1/4 ML but become minority species at higher coverages, when *AcO* and AcO* are equilibrated (Step 3 in Scheme 5). Rate and infrared data showed that K_1 values did not

depend on coverage (Sections 3.2 and 3.3), consistent with the prevalence of AcO* species and their slow interconversion to *AcO* during ketonization catalysis.

DFT treatments were also used to assess the relative rates of AcO* conversion to *AcO* (via Step 2, Scheme 5) and to ketonization products (via Steps 3–13, Scheme 5). The rate of formation of *AcO* from AcO* (r_{*AcO*}) is given by

$$\frac{r_{*AcO*}}{[L]} = \vec{k}_2 \, \theta_{AcO*} \, \theta_* \tag{16}$$

where $[L]$ is the number of catalytically relevant Ti—O pairs, θ_{AcO*} and θ_* are the respective fractional coverages of AcO* and unoccupied Ti—O pairs (*), and $\vec{k}_2$ is the forward rate constant for Step 2 in Scheme 5. Ketonization rates (r_{keto}), in contrast, involve bimolecular reactions between vicinal AcO* species at rates limited by C—C coupling between AcO* and a 1-hydroxy enolate (Step 4, Scheme 5), as shown by kinetic and isotopic data (Section 3.2) and DFT methods (shown next). Ketonization rates are given by

$$\frac{r_{keto}}{[L]} = \vec{k}_4 \, K_1 K_3 \, \theta_{AcO*} \, \theta_* \, P_{AcOH} \tag{17}$$

where $[L]$, θ_{AcO*} and θ_* are as defined above, P_{AcOH} is the ethanoic acid pressure, and $\vec{k}_x$ and K_x are the respective rate constant and equilibrium constant for Step x in Scheme 5. Eqs. (16) and (17) give the ratio of ketonization to *AcO* formation rates (r_{keto}/r_{*AcO*}):

$$\frac{r_{keto}}{r_{*AcO*}} = \frac{\vec{k}_4 \, K_1 K_3}{\vec{k}_2} P_{AcOH} \tag{18}$$

As shown in Scheme 10, these (r_{keto}/r_{*AcO*}) ratios reflect the free energy difference ($\Delta G^{\ddagger}_{keto-*AcO*}$, Eqs. (19) and (20)) between the TS for the C—C coupling step ($G^{\ddagger}_{CC}$, Step 4 in Scheme 5) and the sum of the TS for *AcO* formation from AcO* ($G^{\ddagger}_{*AcO*}$, Step 2 in Scheme 5) and a gaseous ethanoic acid (G_{AcOH}):

$$\frac{r_{keto}}{r_{*AcO*}} = \exp(-\Delta G^{\ddagger}_{keto-*AcO*}/RT) P_{AcOH} \tag{19}$$

$$\Delta G^{\ddagger}_{keto-*AcO*} = G^{\ddagger}_{CC} - G^{\ddagger}_{*AcO*} - G_{AcOH} \tag{20}$$

The DFT-derived $\Delta G^{\ddagger}_{keto-*AcO*}$ value for AcO* bound at Ti_{5c}—O_{2c} pairs on $TiO_2(a)$ (1 0 1) is 45 kJ mol⁻¹ (523 K, 1 bar ethanoic acid). The TS for *AcO* formation and its free energy are shown in Sec-
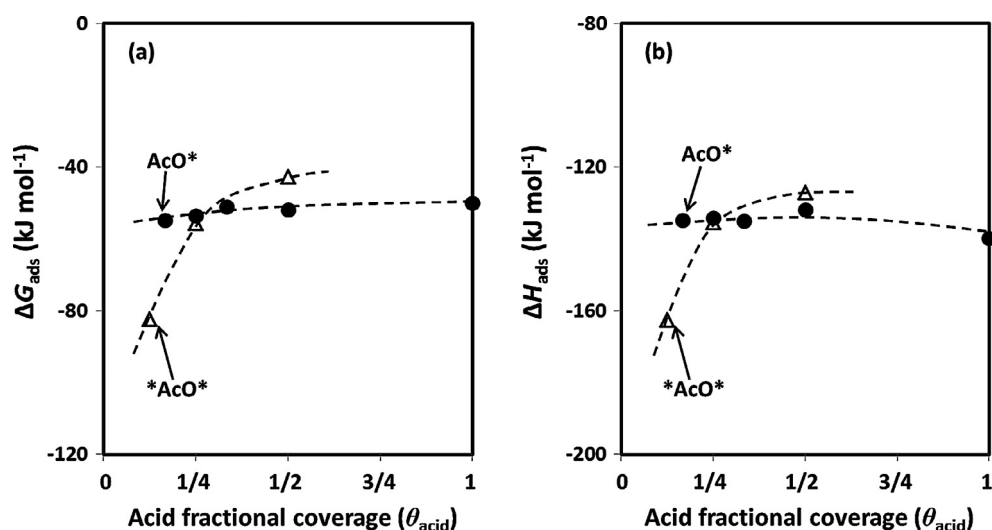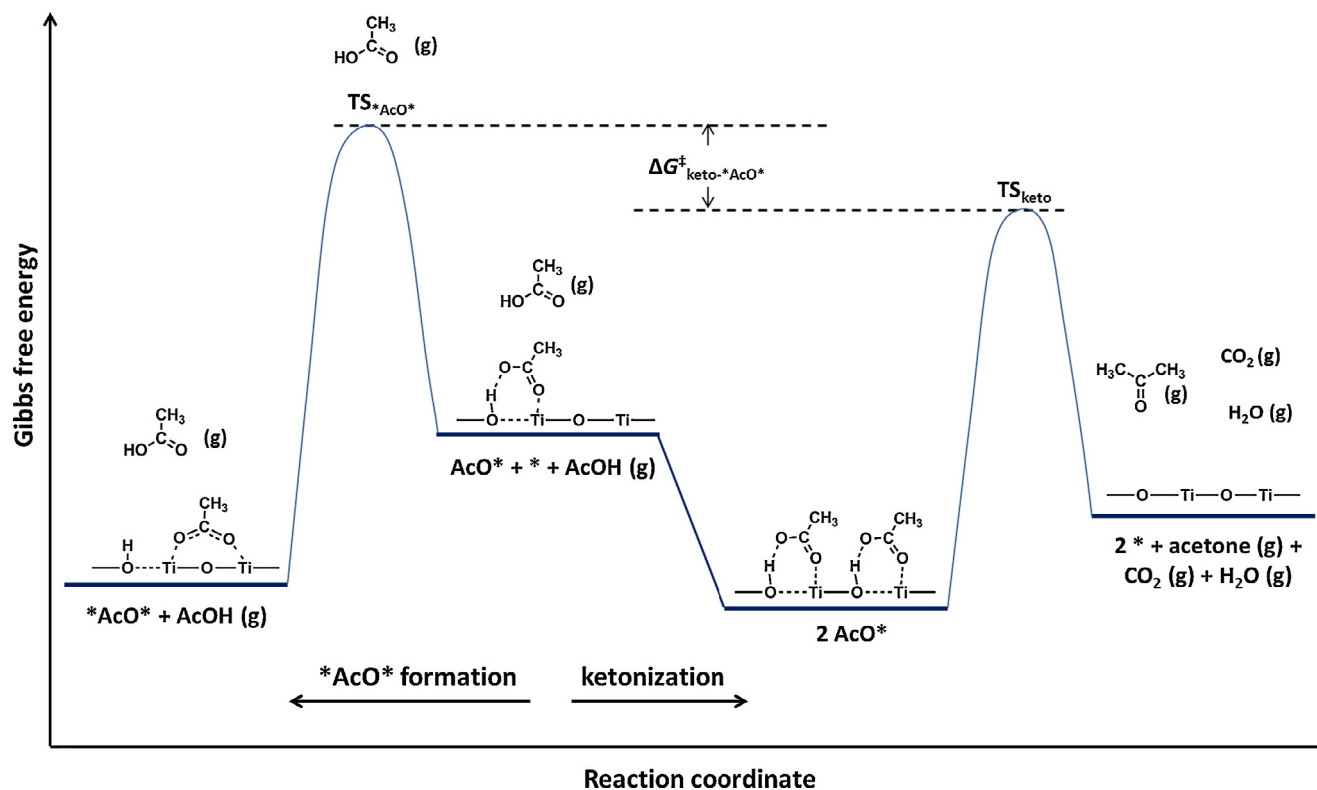

Fig. 7. DFT-derived (a) adsorption free energy (ΔG_{ads}) and (b) its enthalpy component (ΔH_{ads}) as a function of acid fractional coverage (θ_{acid}; Eq. (15)) for AcO* (●) and *AcO* (△) on $TiO_2(a)$ (1 0 1) surfaces (PBE + D3BJ, PAW, 523 K, 1 bar ethanoic acid). Dashed lines indicate qualitative trends.

Scheme 10. Schematic reaction coordinate diagram for ketonization and formation of bidentate carboxylates (*AcO*) from monodentate carboxylates (AcO*) on TiO₂.

tion S14 (SI), while the structure and free energy of the C—C coupling TS are shown below. These free energies lead to (r_{keto}/r_{*AcO*}) ratios much smaller than unity at all pressures and temperatures of interest (Section S15, SI). Thus, DFT methods indicate that *AcO*-AcO* equilibration should occur in the timescale of ketonization turnovers, in contradiction to the slow formation and desorption of *AcO* evident from infrared spectra (Section 3.3), the formation of acetaldehyde and the inhibition of deactivation when H₂ and a Cu function are used (Section 3.1), and the nature of the treatments required to fully recover initial rates after significant deactivation (in the absence of Cu and H₂; Section 3.1).

The Grimme's D3BJ dispersion component in the PBE functionals [43,44] used in these DFT treatments to account for long and intermediate range van der Waals attractive interactions tends to overestimate the binding of adsorbed species, in this case the binding of acid-derived species at Ti—O pairs; this is evident from DFT-derived AcO* formation free energies (−50 to −55 kJ mol⁻¹, Fig. 7a) that are much more negative than measured values (−33 kJ mol⁻¹, Table 2) at the high coverages prevalent in ketonization catalysis (0.70–0.99 ML, 523 K). We expect that the binding of the *AcO* formation and the C—C coupling transition states will also be overestimated by these functionals, which would be more consequential for TS structures that have incipiently formed or cleaved bonds to the Ti—O pairs with a longer bond distance.

The *AcO* formation TS involves the incipient formation of a new Ti—O bond as AcO* reacts with a Ti center (Ti—O bond distance: 0.290 nm at TS, 0.209 nm in *AcO* products, Scheme S4, SI). In contrast, the C—C coupling TS involves the cleavage of a Ti—O bond in a bound AcO* as it forms the 1-hydroxy enolate and then a TS with a longer Ti—O bond (0.189 nm, Scheme 11b) than in 1-hydroxy enolate (0.185 nm). The distance of the incipiently formed Ti—O bond at the *AcO* formation TS is much longer than the one incipiently cleaved at the C—C coupling TS (0.290 vs. 0.189 nm), indicating the overbinding tendency is more conse-

quential for the *AcO* formation TS. As a result, the free energy for the *AcO* formation TS ($G^{‡}_{*AcO*}$) is expected to be underestimated more than that for the C—C coupling TS ($G^{‡}_{CC}$), leading to the overestimation for $\Delta G^{‡}_{keto-*AcO*}$ values (Eq. (20)). As shown next, such overbinding tendencies influence the C—C coupling TS and the bound reactants (two adjacent AcO*) similarly; their free energy difference ($\Delta G^{‡}_{CC}$, Eq. (11)) is thus nearly independent of the overbinding tendencies and can be used for the benchmarking between experiment and theory.

DFT-derived ΔG_{ads} values show that bidentate *AcO* species at Ti_{5c}—O_{2c} pairs on TiO₂(r) (110) become less stable with increasing acid coverage (θ_{acid}) up to saturation coverages (1/2 ML) (Fig. 8a; ΔH_{ads} components depicted in Fig. 8b), as found also on TiO₂(a) (101) (Fig. 7a). These ΔG_{ads} values for *AcO* are more negative on TiO₂(r) (110) than on TiO₂(a) (101) (e.g. −72 vs. −43 kJ mol⁻¹, 1/2 ML *AcO*, 523 K, 1 bar, Figs. 7a and 8a), as a result of shorter Ti_{5c}—Ti_{5c} distances on TiO₂(r) (110) than on TiO₂(a) (101) surfaces ($d_{Ti5c—Ti5c}$ 0.299 vs. 0.383 nm, Table 5); these Ti_{5c}—Ti_{5c} distances on TiO₂(r) (110) match more closely the O—O distances in *AcO* species ($d_{O—O}$ 0.230 nm, Schemes 9f), thus providing more effective orbital overlap.

The DFT-derived ΔG_{ads} values for AcOH* species on TiO₂(r) (110) also become less negative from −59 kJ mol⁻¹ (1/4 ML) to −53 kJ mol⁻¹ (1/2 ML) and then to −11 kJ mol⁻¹ at saturation coverages (1 ML, Fig. 8a), in contrast to the much smaller ΔG_{ads} change on TiO₂(a) (101) in the same range of coverages (−54 to −50 kJ mol⁻¹, Fig. 7a). This stronger influence of coverages on the stability of monodentate modes on TiO₂(r) (110), especially at θ_{acid} above 1/2 ML, is indicative of strong steric repulsion between monodentate species bound to vicinal Ti_{5c}—O_{2c} pairs in TiO₂(r) (110), with its shorter Ti_{5c}—Ti_{5c} distances than in TiO₂(a) (101). As expected from such repulsion, the effect of acid coverage predominantly reflects the enthalpic component of ΔG_{ads} (Fig. 8b). The preference for *AcO* over AcOH* on TiO₂(r) surfaces at all acid

coverages (Fig. 8a) is consistent with the absence of detectable AcOH* bands in the infrared spectrum of $TiO_2(r)$ during ethanoic acid ketonization reactions (Fig. 5b, Section 3.3).

The proposed elementary steps for ethanoic acid ketonization (Scheme 5) were examined on $TiO_2(a)$ (1 0 1) surfaces at 1 ML AcO* coverages (θ_{acid}, Eq. (15)) using DFT methods; such high coverages seek to rigorously account for the saturated surfaces prevalent during catalysis. The first step involves the cleavage of the α-C—H bond in AcO* to form 1-hydroxy enolates (Step 3 in Scheme 5). The H-atom is abstracted by the vicinal O_{2c} site; the α-H—O_{2c} distance is 0.113 nm and the α-C—H distance is 0.150 nm at the TS that mediates the formation of the 1-hydroxy enolate (Scheme 11a). The similar α-H—O_{2c} distances at the TS and in the bound 1-hydroxy enolate (0.113 vs. 0.110 nm) demonstrate the late nature of the enolate formation TS on $TiO_2(a)$ (1 0 1); such a late TS reflects the strong α-C—H bond in carboxylic acids and the endothermic nature of such elementary steps. The transition states for enolate formation from carbonyl compounds in aldol condensation reactions on $TiO_2(a)$ (1 0 1) occur earlier along the reaction coordinate than for acid reactants because the α-C—H bonds are weaker in carbonyl compounds than in carboxylic acids [24].

1-Hydroxy enolates can attack the carboxylic C-atom in a vicinal AcO* via its nucleophilic β-C-atom to form a new C—C bond (Step 4, Scheme 5). The two C-atoms lie farther apart at the TS (0.234 nm, Scheme 11b) than in the product state (0.150 nm), but are closer than their combined van der Waals radii (0.340 nm), indicating that the C—C coupling TS lies at an intermediate point along the reaction coordinate. The OH group in the acid moiety of the C—C coupling TS structure is stabilized by H-bonding with a neighboring lattice O_{2c} atom and with the bound OH species formed via dissociation of coadsorbed ethanoic acid to form AcO* at vicinal Ti_{5c}—O_{2c} pairs (Scheme 11b).

The α-hydroxy γ-carboxy alkoxide formed via C—C coupling undergoes an intramolecular H-shift mediated by the $TiO_2(a)$ (1 0 1) surface to form a β-keto carboxylate and $H_2O(g)$ (Steps 5–7, Scheme 5). The carboxyl H-atom in the alkoxide first transfers to a vicinal O_{2c} (Step 5, Scheme 5); this TS occurs very early along the reaction coordinate, as evidenced by the similar carboxyl O—H bond lengths in the reactant and the TS (0.104 vs. 0.105 nm, Scheme 11c). The H-shift TS is stabilized by interactions with the bound OH species derived from coadsorbed AcO* (Scheme 11c). The H-atom that shifts to the O_{2c} site then combines with the α-OH group in the alkoxide to form H_2O (Step 6, Scheme 5). This latter step is mediated by a late TS with a nearly-formed H_2O molecule at the TS (TS structures in Section S16, SI), consistent with the endothermic nature of this reaction (+94 kJ mol^{-1}, 523 K, Section S17, SI).

The β-keto carboxylate species then reprotonates to form a β-keto acid (Step 8, Scheme 5), which decarboxylates to propen-2-olate and CO_2 (Steps 9–11, Scheme 5). The C—C bond between the carboxylate and the enolate moiety at the decarboxylation TS (d_{C-C} = 0.243 nm; Scheme 11d) is longer than that in the β-keto carboxylate reactant (d_{C-C} = 0.152 nm). The elongation of this C—C bond at the decarboxylation TS is consistent with the sequential nature of the formation of the H_2O and CO_2 decomposition products (Steps 5–10, Scheme 5) and indicative of the stable nature of discrete β-keto carboxylate intermediates formed via endothermic dehydration steps (Steps 5–6, Scheme 5) on $TiO_2(a)$ (1 0 1).
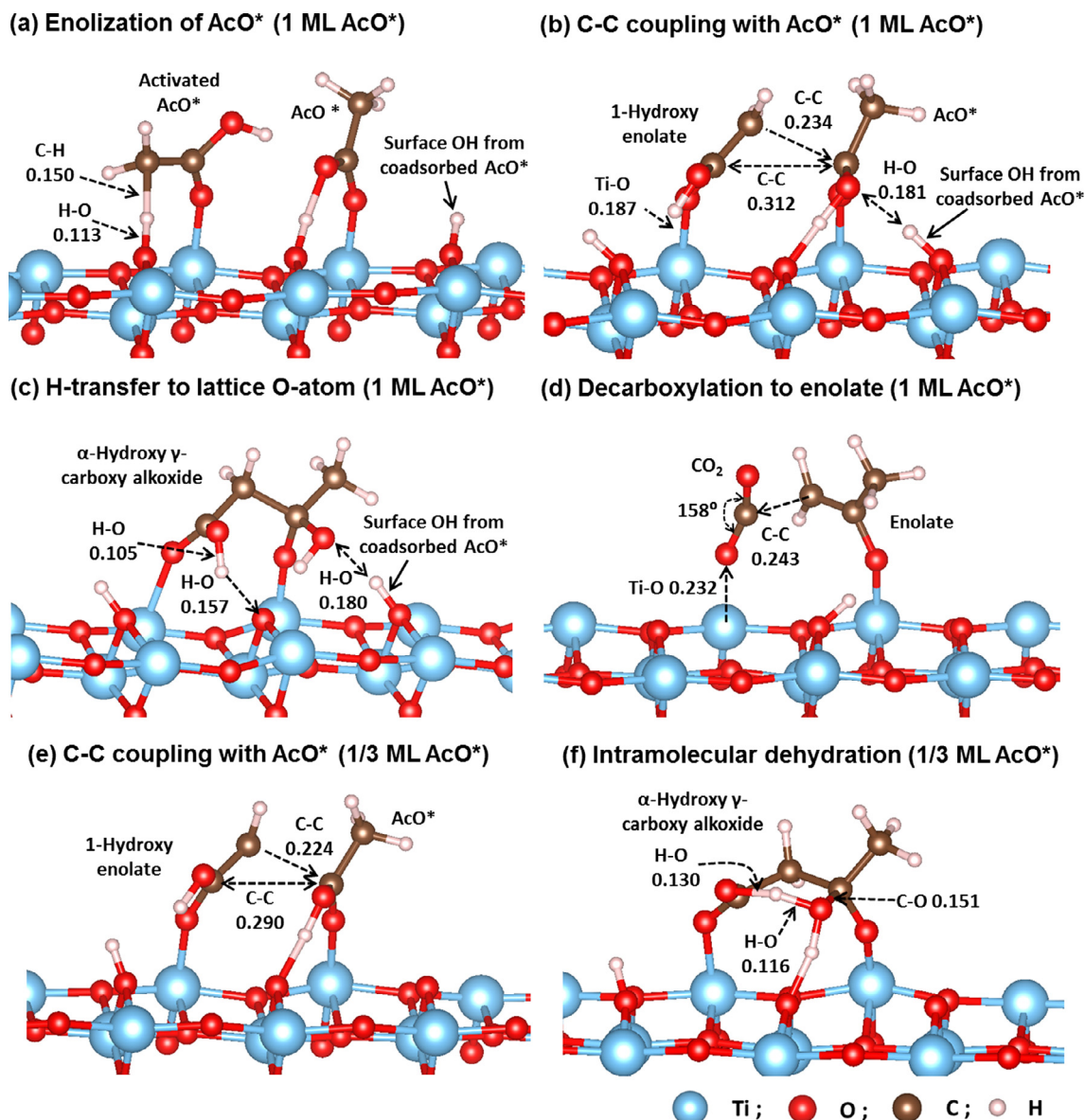
The propen-2-olate product formed in the decarboxylation of β-keto carboxylates (Step 10, Scheme 5) reprotonates to form acetone (Step 12, Scheme 5). The TS structure (Section S16, SI) resembles that for enolate formation from AcO* in its ketonization reactions (Scheme 11a), but with a shorter α-C—H and a longer α-H—O_{2c} bond (0.148 vs. 0.150 nm, 0.114 vs. 0.113 nm, respectively). Acetone desorption (Step 13, Scheme 5) then completes the catalytic ketonization turnover on $TiO_2(a)$ surfaces.

Fig. 9 depicts free energies along the reaction coordinate for the ketonization elementary steps in Scheme 5 (523 K, 1 bar ethanoic acid, 1 ML AcO*) relative to two gaseous ethanoic acids and a bare $TiO_2(a)$ surface (enthalpies and entropies; Section S17, SI). AcO* species exhibit the lowest free energy among adsorbed species, consistent with AcO* as the most abundant surface intermediate (MASI). DFT-derived adsorption free energies for AcO* (ΔG_{AcO^*}, −50 kJ mol^{-1}, Eq. (10); Fig. 9) are slightly more negative than measured values (−33 ± 1 kJ mol^{-1}, Table 3), a trend that reflects the overbinding tendencies of the Grimme's D3BJ dispersion corrections in PBE functionals [43,44]; this is also evident from the more negative ΔH_{AcO^*} values derived from theory (−140 kJ mol^{-1}, Table 6) compared with those obtained from the regression of the temperature dependence of measured K_1 values (−114 ± 3 kJ mol^{-1}, Table 3).

The C—C coupling TS (TS_4 in Fig. 9; Step 4, Scheme 5) gives the highest free energy along the reaction coordinate, consistent with its kinetic relevance in ketonization reactions on $TiO_2(a)$. The DFT-derived $\Delta G_{CC,a}^{\ddagger}$ value (Eq. (14)), given by the difference between the free energies of the C—C coupling TS and two bound AcO* species, is 160 kJ mol^{-1} (523 K, 1 bar ethanoic acid, 1 ML AcO*; Table 6); its respective enthalpy and entropy components ($\Delta H_{CC,a}^{\ddagger}$, $\Delta S_{CC,a}^{\ddagger}$) are 128 kJ mol^{-1} and −63 J mol^{-1} K^{-1} (Table 6). Measured $\Delta G_{CC,a}^{\ddagger}$, $\Delta H_{CC,a}^{\ddagger}$ and $\Delta S_{CC,a}^{\ddagger}$ values are 166 ± 1 kJ mol^{-1}, 137 ± 1 kJ mol^{-1}, and −56 ± 1 J mol^{-1} K^{-1} (Tables 2 and 3), in good agreement with these DFT estimates. The $\Delta H_{CC,a}^{\ddagger}$ difference between DFT-derived and measured values (9 kJ mol^{-1}) is much smaller than for ΔH_{AcO^*} (27 kJ mol^{-1}), because overbinding tendencies influence the bound reactant and TS for $\Delta H_{CC,a}^{\ddagger}$, but only the product state in the case of ΔH_{AcO^*}. DFT-derived kinetic isotope effects for the C—C coupling step ($\overleftarrow{k_4}K_3$, Eq. (13)) and thermodynamic isotope effects for ethanoic acid dissociation to AcO* (K_1, Eq. (9)) are both near unity (($\overleftarrow{k_4}K_3$)$_H$/($\overleftarrow{k_4}K_3$)$_D$ = 1.1, $(K_1)_H/(K_1)_D$ = 0.9; 523 K, Table 6), in agreement with experiments (($\overleftarrow{k_4}K_3$)$_H$/($\overleftarrow{k_4}K_3$)$_D$ = 1.1, $(K_1)_H/(K_1)_D$ = 1.0; 523 K, Table 2).

DFT-derived structures for bound intermediates and transition states in Scheme 5 are similar at 1/3 ML and 1 ML AcO* coverages. The C—C bond at the C—C coupling TS (Step 4, Scheme 5) is only slightly shorter at 1/3 ML (0.224 nm, Scheme 11e) than at 1 ML (0.234 nm, Scheme 11b). DFT-derived free energies along the reaction coordinate (Section S18, SI) show that AcO* remains the MASI and the C—C coupling remains the kinetically-relevant step at both coverages. The $\Delta G_{CC,a}^{\ddagger}$ value, however, is larger at lower coverages (181 vs. 160 kJ mol^{-1}, Table 6), a difference that predominantly reflects the stabilizing effects of H-bonding on $\Delta H_{CC,a}^{\ddagger}$ at higher coverages (149 vs. 128 kJ mol^{-1}, Table 6). We conclude that the prevalent high acid coverages are requisite for ketonization catalysis because of the preferential stabilization of the C—C bond formation TS over its relevant precursors on $TiO_2(a)$ (1 0 1) by H-bonding, which become most evident at near-saturation coverages. Such coverage effects provide yet another demonstration of how dense monolayers allow facile turnovers for reactions that would proceed much more slowly, or not at all, at lower coverages, because crowded surfaces favor TS structures over those of the relevant precursors [57].

A concerted form of the two-step H_2O elimination reaction (Steps 5–6, Scheme 5) of α-hydroxy γ-carboxy alkoxide species (formed in the C—C coupling step) to β-keto carboxylates becomes kinetically-accessible only at low acid coverages (1/3 ML AcO*, Scheme 12). This concerted route is mediated by a six-membered ring TS (Scheme 11f) and involves a direct shift of the carboxyl H-atom to the leaving α-OH group. This route exhibits a slightly lower free energy at the TS than for the H_2O formation TS involved in the two-step route (Step 6, Scheme 5), but only at acid coverages much lower than those prevalent during practical ketonization catalysis (65 vs. 69 kJ mol^{-1}, 1/3 ML, Section S18, SI). The concerted

(a) Enolization of AcO* (1 ML AcO*)

(b) C-C coupling with AcO* (1 ML AcO*)

(c) H-transfer to lattice O-atom (1 ML AcO*)

(d) Decarboxylation to enolate (1 ML AcO*)

(e) C-C coupling with AcO* (1/3 ML AcO*)

(f) Intramolecular dehydration (1/3 ML AcO*)

Ti ; O ; C ; H

Scheme 11. DFT-derived transition state structures involved in ethanoic acid ketonization on $TiO_2(a)(101)$ surfaces (PBE + D3BJ, PAW). Spectator coadsorbed acids are not shown for clarity; distances are given in nm.

route becomes favored at low coverages, which cannot provide the H-bonding interactions that favor the sequential two-step pathways. This concerted route, however, was not considered in previous studies [3,19], in which theoretical treatments were implemented on essentially bare surfaces.

The ketonization elementary steps in Scheme 5 were also examined on coordinatively-unsaturated Ti_{5c}–O_{2c} pairs at $TiO_2(r)(110)$ surfaces. AcOH* is the stable monodentate form of adsorbed ethanoic acid at Ti_{5c}–O_{2c} pairs on $TiO_2(r)$ surfaces (Scheme 9e), in contrast to the dissociated AcO* species that prevail on $TiO_2(a)(101)$ (Schemes 9b and c). These AcOH* species are much less stable, however, than bidentate carboxylates (*AcO*) on $TiO_2(r)(110)$ (Fig. 8). $TiO_2(r)$ surfaces thus prefer to saturate with *AcO*. The free energies for *AcO* on $TiO_2(r)(110)$ (−72 kJ mol^{-1}, 523 K, 1 bar ethanoic acid, with respect to gaseous ethanoic acid reactants and a $TiO_2(r)$ surface henceforth) were more negative than those for other intermediates or transition states along the ketonization coordinate (Fig. 10; discussed in detail below), indicating that *AcO* is the MASI on $TiO_2(r)(110)$ at ketonization conditions.

These theoretical conclusions are consistent with the infrared spectra obtained from $TiO_2(r)$ samples during ethanoic acid ketonization catalysis (Section 3.3).

The formations of 1-hydroxy enolates from monodentate and bidentate forms of adsorbed ethanoic acids on $TiO_2(r)(110)$ (AcOH* and *AcO* in this case) were both examined. The enolization of AcOH* at a Ti_{5c}–O_{2c} pair on $TiO_2(r)(110)$ involves TS structures (Scheme 13a) similar to those on $TiO_2(a)(110)$ (Scheme 11a). The abstracted α-H-atom at the TS on $TiO_2(r)(110)$ is slightly closer to the O_{2c} site and farther from the α-C atom than on $TiO_2(a)(101)$ (0.109 vs. 0.113 nm, 0.162 vs. 0.150 nm, Schemes 11a and 13a). This later TS on $TiO_2(r)(110)$ is consistent with the weaker basicity of O_{2c} sites on $TiO_2(r)(110)$ than on $TiO_2(a)(101)$ (E_{PA} −1093 vs. −1175 kJ mol^{-1}, Table 5). In contrast to AcOH*, *AcO* binds to two neighboring Ti_{5c} centers via its two O-atoms before its α-H-atom is abstracted by a vicinal O_{2c} site (Scheme 13b). The enolization TS of *AcO* has a more negative enthalpy than for AcOH* (−45 vs. −33 kJ mol^{-1}, 523 K, 1/2 ML *AcO*, Section S19, SI), but also a larger entropy loss (−229 vs. −192 J mol^{-1}
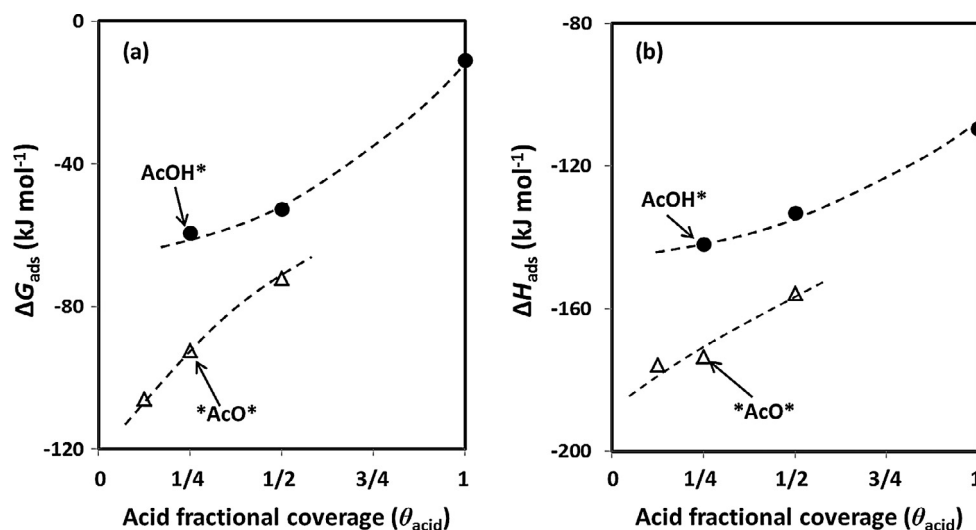
Fig. 8. DFT-derived (a) adsorption free energy (ΔG_{ads}) and (b) its enthalpy component (ΔH_{ads}) as a function of acid fractional coverage (θ_{acid}; Eq. (15)) for AcOH* (●) and *AcO* (△) on TiO_2(r) (1 1 0) surfaces (PBE + D3BJ, PAW, 523 K, 1 bar ethanoic acid). Dashed lines indicate qualitative trends.

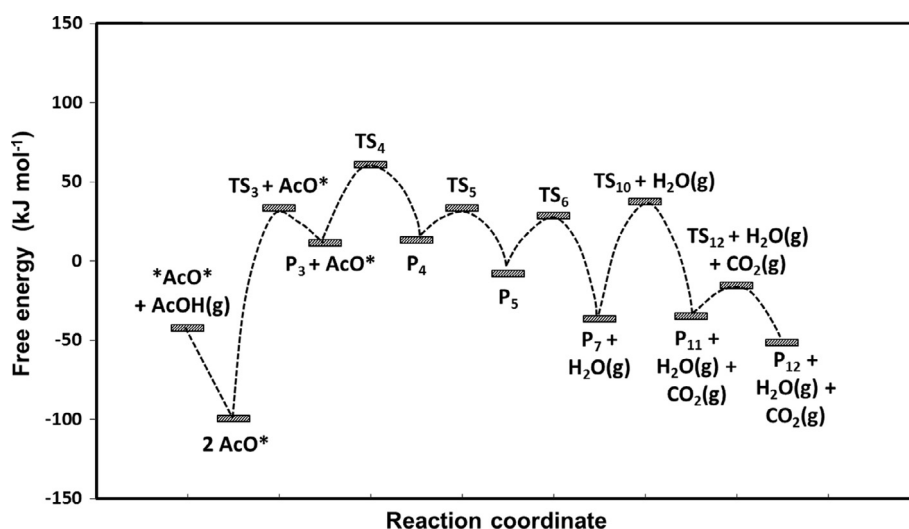**Fig. 9.** DFT-derived free energy reaction coordinate diagram for ethanoic acid ketonization on TiO_2(a) (1 0 1) surfaces (PBE + D3BJ, PAW; 523 K, 1 bar ethanoic acid, 1 ML AcO*). All energy values are reference to two gaseous ethanoic acid reactants and a bare TiO_2(a) surface, which defines the zero energy point in the ordinate. Only key surface intermediates and transition states are shown for clarity. TS_x and P_x represent the transition state and product of Step x in Scheme 5, respectively.

Table 6
DFT-derived ΔG_{AcO^*}, $\Delta G^{\ddagger}_{CC,a}$ and corresponding enthalpy and entropy components and isotope effects for ethanoic acid ketonization on TiO_2(a) (1 0 1) surfaces at 1 ML and 1/3 ML AcO* coverages.[a]

θ_{acid} (ML)	ΔH_{AcO^*} (kJ mol^{-1})	ΔS_{AcO^*} (J mol^{-1} K^{-1})	ΔG_{AcO^*} (kJ mol^{-1})	$\Delta H^{\ddagger}_{CC,a}$ (kJ mol^{-1})	$\Delta S^{\ddagger}_{CC,a}$ (J mol^{-1} K^{-1})	$\Delta G^{\ddagger}_{CC,a}$ (kJ mol^{-1})	$\frac{(K_1)_H}{(K_1)_D}$	$\frac{(k_4 K3)_H}{(k_4 xK3)_D}$
1	−140	−172	−50	128	−63	160	0.9	1.1
1/3	−135	−160	−51	149	−60	181	0.9	1.1

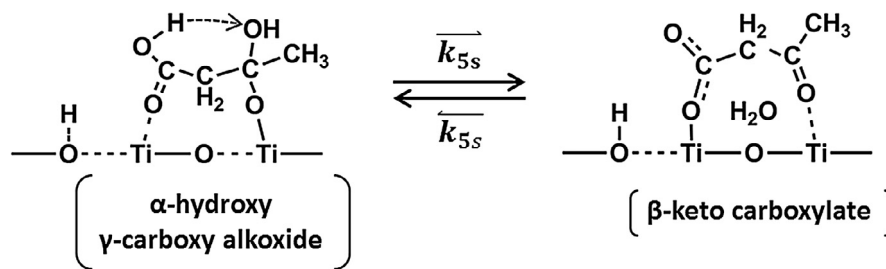[a] PBE + D3BJ, PAW, 523 K, 1 bar ethanoic acid.

K^{-1}, Section S19, SI); these differences lead to a higher free energy for the enolization TS of *AcO* than that of AcOH* (75 vs. 67 kJ mol^{-1}), indicating the more strongly bound *AcO* species are less reactive than AcOH* in the formation of 1-hydroxy enolates.

The 1-hydroxy enolates nucleophilically attack another AcOH* coadsorbed at a vicinal Ti_{5c}—O_{2c} pair to form a new C—C bond (Step 4, Scheme 5). The incipient C—C bond at the C—C coupling TS on TiO_2(r) (1 1 0) has a distance of 0.238 nm (Scheme 12c), similar

with that on TiO_2(a) (1 0 1) (0.234 nm, Scheme 10b). DFT-derived enthalpies for this TS, however, are much less negative on TiO_2(r) (1 1 0) than on TiO_2(a) (1 0 1) (−116 vs. −152 kJ mol^{-1}, 523 K, referenced to two gaseous AcOH reactants and a bare TiO_2(r)/TiO_2(a) surface, Sections S16 and S18, SI); these less favorable enthalpies lead, in turn, to much higher TS free energies on TiO_2(r) (1 1 0) (97 kJ mol^{-1}, Fig. 10) than on TiO_2(a) (1 0 1) (61 kJ mol^{-1}, Fig. 9). The less stable C—C coupling TS structures on TiO_2(r) (1 1 0) reflect, in part, stronger repulsive interactions between the bound

5s. Intramolecular dehydration of α-hydroxy γ-carboxy alkoxide to form β-keto carboxylate

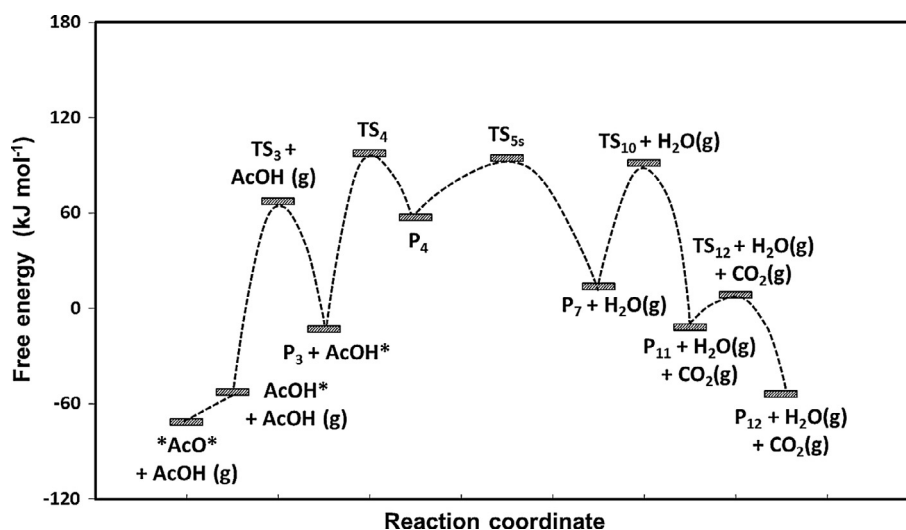**Scheme 12.** Direct intramolecular dehydration of α-hydroxy γ-carboxy alkoxide.

Fig. 10. DFT-derived free energy reaction coordinate diagram for ethanoic acid ketonization on $TiO_2(r)$ $(1\,1\,0)$ surfaces (PBE + D3BJ, PAW; 523 K, 1 bar ethanoic acid, 1/2 ML *AcO*). All energy values are relative to two gaseous ethanoic acid reactants and a bare TiO_2 surface, which defines the zero energy point in the ordinate. Only key surface intermediates and transition states are shown for clarity. TS_x and P_x represent the transition state and product of Step x in Scheme 5, respectively, except TS_{5s} that represents the transition state of Step 5s in Scheme 12.

1-hydroxy enolate and the coadsorbed AcOH* reactants at the TS, because of the closer Ti_{5c}—Ti_{5c} centers on $TiO_2(r)$ $(1\,1\,0)$; they also reflect the absence of H-bonding between the C—C coupling TS and surface OH species derived from *AcO* bound at neighboring Ti_{5c}—O_{2c} pairs, as a result of the longer Ti_{5c}—O_{2c} distance on $TiO_2(r)$ $(1\,1\,0)$, which places surface OH species farther from the C—C coupling TS (Scheme 13c).

The subsequent dehydration of the C—C coupling products (α-hydroxy γ-carboxy alkoxide species) to β-keto carboxylates preferentially occurs via the concerted six-membered ring TS route (Scheme 12) on $TiO_2(r)$ $(1\,1\,0)$ (Scheme 13d; free energy 94 kJ mol^{-1}, 523 K, 1 bar ethanoic acid, Fig. 10), as also found, but only at 1/3 ML coverages, on $TiO_2(a)$ $(1\,0\,1)$ (Scheme 11f). In contrast, the two-step intramolecular H-shift pathway (Steps 5–6, Scheme 5), mediated by O_{2c} sites, is unfeasible on $TiO_2(r)$ $(1\,1\,0)$, as shown by the high TS free energies for the H-shift from the carboxyl group in alkoxides to a vicinal O_{2c} site (>150 kJ mol^{-1}, 523 K, 1 bar ethanoic acid; Step 5, Scheme 5). Such high free energies reflect the weakly basic O_{2c} sites on $TiO_2(r)$ $(1\,1\,0)$, as well as the lack of H-bonding stabilization by neighboring surface OH species, which also leads to the high TS free energies for the C—C coupling steps on TiO_2 (r) as discussed above (Scheme 13c).

Decarboxylation and reprotonation of the β-keto carboxylate dehydration products form acetone and CO_2 (Steps 10–14, Scheme 5), which complete the ketonization turnover on $TiO_2(r)$

surfaces. DFT-derived structures of reactants, transition states, and products involved in these steps also resemble those on $TiO_2(a)$ $(1\,0\,1)$.

The C—C coupling TS (Step 4, Scheme 5) has the highest free energy along the ketonization pathway on $TiO_2(r)$ $(1\,1\,0)$ (523 K, 1 bar ethanoic acid, with respect to two gaseous ethanoic acid reactants and a bare $TiO_2(r)$ surface, Fig. 10), indicating that the ketonization rates on $TiO_2(r)$ $(1\,1\,0)$ are limited by the C—C coupling step between 1-hydroxy enolates and coadsorbed acids. Ketonization rates on saturated $TiO_2(r)$ $(1\,1\,0)$ surfaces, prevalent at ketonization conditions as evident from infrared spectra (Section 3.3), can thus be described as

$$\frac{r}{[L]} = \frac{k_B T}{2h} \exp(-\Delta G^{\ddagger}_{CC,r}/RT)P_{acid} \qquad (21)$$

where $[L]$ is the number of catalytically-relevant Ti—O pairs on $TiO_2(r)$ $(1\,1\,0)$; $\Delta G^{\ddagger}_{CC,r}$ represents the free energy of the C—C coupling TS ($G^{\ddagger}_{CC}$) on $TiO_2(r)$ $(1\,1\,0)$ with respect to a bound *AcO* species (G_{*AcO*}) and a gaseous acid reactant (G_{acid}):

$$\Delta G^{\ddagger}_{CC,r} = G^{\ddagger}_{CC} - G_{*AcO*} - G_{acid} \qquad (22)$$

DFT-derived $\Delta G^{\ddagger}_{CC,r}$ value is 169 kJ mol^{-1} (523 K, 1 bar ethanoic acid, Fig. 10), leading to ketonization turnover rates that linearly increase from 7.3×10^{-8} to 2.2×10^{-6} (Ti—O)$^{-1}$ s^{-1} as the pressure
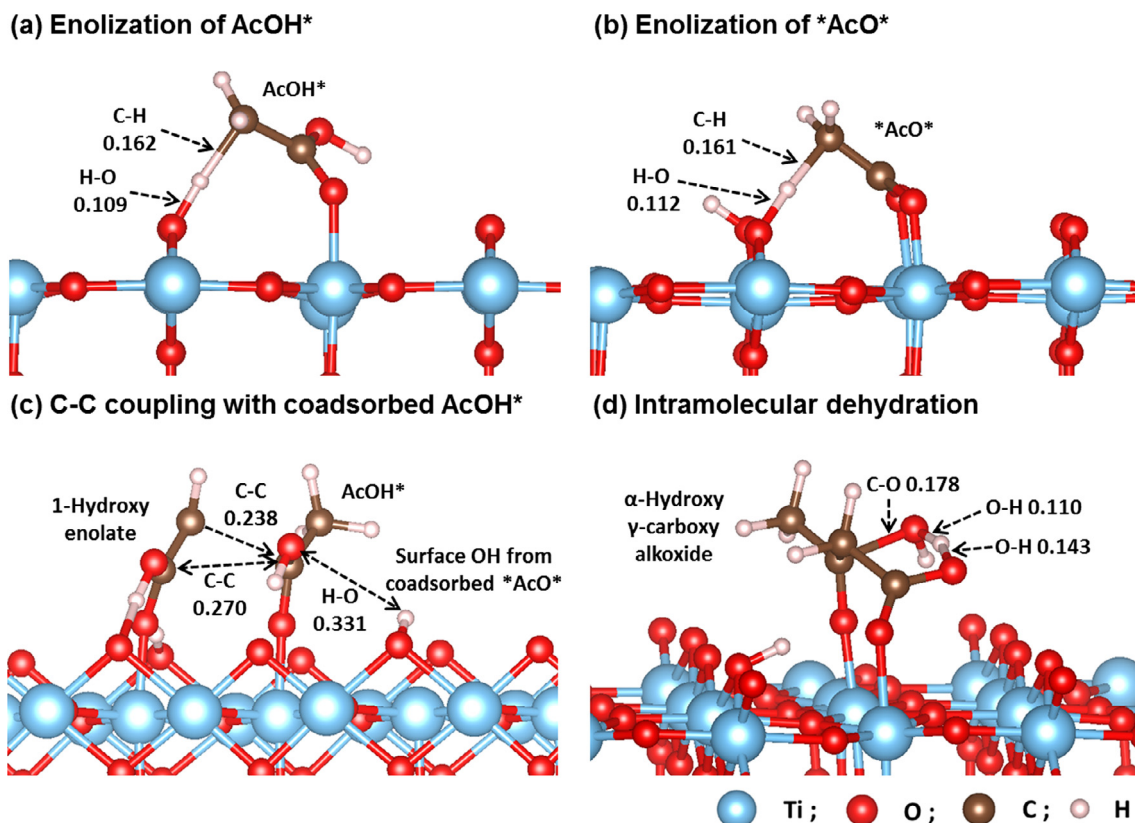
Scheme 13. DFT-derived transition state structures involved in ethanoic acid ketonization on $TiO_2(r)$ $(1\,1\,0)$ surfaces (PBE + D3BJ, PAW, 1/2 ML *AcO*). Spectator coadsorbed acids are not shown for clarity.

of ethanoic acid increases within 0.1–3.0 kPa at 523 K (Eq. (21)). Such a first-order kinetic dependence on ethanoic acid pressure is inconsistent with the functional form of Eq. (7), which accurately describes the measured ketonization rates on $TiO_2(r)$ within the same pressure range (Fig. 4); the respective ketonization turnover rates (7.3×10^{-8}–2.2×10^{-6} $(Ti\!-\!O)^{-1}$ s^{-1}) estimated from the DFT treatments are also much lower than the experimentally-measured values (4.3×10^{-6}–3.0×10^{-5} $(Ti\!-\!O)^{-1}$ s^{-1}, Fig. 4). These DFT calculations thus provide evidence that the majority $TiO_2(r)$ surfaces are inactive for ketonization and that the minority sites or residual $TiO_2(a)$ surfaces present in the $TiO_2(r)$ powders account for the measured ketonization rates.

The above theoretical treatments and their accurate benchmarking with experiments shed light into the underpinning geometric factors that lead to marked reactivity differences between rutile and anatase TiO_2 surfaces. Specifically, the identity and binding properties of the prevalent forms of dissociated acid reactants and their reactivity in ketonization depend on the local extended coordination of coordinatively-unsaturated $Ti_{5c}\!-\!O_{2c}$ pairs. The concerted stabilization of the relevant $C\!-\!C$ bond formation transition states leads to compensation effects that attenuate the differences in acid strength of the Ti_{5c} centers and in basicity of the O_{2c} centers between $Ti_{5c}\!-\!O_{2c}$ pairs on $TiO_2(r)$ $(1\,1\,0)$ and $TiO_2(a)$ $(1\,0\,1)$. Consequently, $Ti_{5c}\!-\!O_{2c}$ and $Ti_{5c}\!-\!Ti_{5c}$ distances are the most accurate descriptors of reactivity for ketonization of carboxylic acids on TiO_2 and account for the very different reactivity of anatase and rutile surfaces.

4. Conclusions

$C_2\!-\!C_4$ carboxylic acids undergo selective ketonization to alkanones, CO_2, and H_2O on TiO_2 and ZrO_2 catalysts at 503–533 K. Coordinatively unsaturated acid-base $M\!-\!O$ (M = Ti, Zr) pairs on these oxides are catalytically relevant for ketonization reactions; the numbers of these pairs were titrated by carboxylic acids during aldol condensation reactions. Ketonization turnover rates are higher on monoclinic ZrO_2 than on tetragonal ZrO_2 and anatase TiO_2 but are much lower on rutile TiO_2. The more active oxides, however, show larger deactivation rate constants. Unreactive bidentate carboxylates, formed gradually from dissociation of carboxylic acids on $M\!-\!O$ pairs, account for the deactivation during steady-state catalysis. Cu co-catalysts and added H_2 scavenge trace levels of gaseous ketene species, present in equilibrium with bidentate carboxylates, via hydrogenation of these ketene species to alkanals and 1-alkanols and thus inhibit deactivation significantly.

Infrared spectra and theoretical treatments show that dissociation of carboxylic acids on anatase TiO_2 surfaces forms monodentate carboxylates each bound on one $Ti\!-\!O$ pair and bidentate carboxylates each bound on two vicinal $Ti\!-\!O$ pairs. The stability of the monodentate carboxylates on anatase TiO_2 surfaces is slightly influenced by the surface coverage, because of the absence of strong repulsive interactions between carboxylates bound to $Ti\!-\!O$ pairs with large distances between nearest Ti centers. The bidentate carboxylates, in contrast, become less stable with increasing acid coverages, as a result of the mismatch between the distances of the $Ti\!-\!Ti$ centers and of the $O\!-\!O$ atoms in the bidentate carboxylates. This difference in the stability dependence on the surface coverage for monodentate and bidentate carboxylates drives a strong preference to crowd anatase TiO_2 surfaces with monodentate carboxylates, which are prevalent at ketonization conditions. In contrast to anatase TiO_2, the closer $Ti\!-\!Ti$ centers on rutile TiO_2 lead to more efficient binding of the two O-atoms in each bidentate carboxylate at these Ti centers and to stronger

steric repulsion between monodentate adsorbed acids bound at vicinal Ti—O pairs. These effects combine to make bidentate carboxylates the predominant adsorbed species on rutile TiO_2.

The C—C coupling of 1-hydroxy enolate species, formed from α-C—H cleavage of monodentate carboxylates or molecularly adsorbed acids, with coadsorbed acids acts as a common kinetically-relevant step for ketonization on anatase and rutile TiO_2 surfaces. The C—C coupling transition state (TS) on anatase TiO_2 becomes more stable relative to its monodentate carboxylate precursors as the coverage of the precursors increases, because of H-bonding between this C—C coupling TS and vicinal surface OH species derived from dissociation of coadsorbed carboxylic acids. Such stabilization via H-bonding also renders a surface-mediated two-step route favorable for the subsequent intramolecular dehydration of the C—C coupling products (α-hydroxy γ-carboxy alkoxides) at high acid coverages. In contrast, a concerted route through a six-membered ring TS prevails for this dehydration reaction at low acid coverages. These H-bonding interactions are absent on rutile TiO_2 surfaces, because of the longer distance between Ti and O sites in Ti—O pairs in rutile TiO_2 than in anatase TiO_2, making bound TS structures and surface OH species farther apart from each other. The closer Ti—Ti centers on rutile TiO_2 lead to steric hindrance between the coreactants at the C—C coupling TS, further rendering rutile TiO_2 much less reactive than anatase TiO_2 in ketonization catalysis. These differences in the stability of surface intermediates and transition states between anatase and rutile TiO_2 surfaces unveil the necessity of moderate distances of acid-base and acid-acid centers for ketonization of carboxylic acids on metal oxides.

Acknowledgments

Appendix A. Supplementary material

Supplementary data associated with this article can be found, in the online version, at http://dx.doi.org/10.1016/j.jcat.2016.11.006.

References

[1] M. Renz, Eur. J. Org. Chem. 2005 (2005) 979–988.
[2] T.N. Pham, T. Sooknoi, S.P. Crossley, D.E. Resasco, ACS Catal. 3 (2013) 2456–2473.
[3] G. Pacchioni, ACS Catal. 4 (2014) 2874–2888.
[4] B. Peng, X. Yuan, C. Zhao, J.A. Lercher, J. Am. Chem. Soc. 134 (2012) 9400–9405.
[5] J. Sun, R.A.L. Baylon, C. Liu, D. Mei, K.J. Martin, P. Venkitasubramanian, Y. Wang, J. Am. Chem. Soc. 138 (2016) 507–517.
[6] C.A. Gaertner, J.C. Serrano-Ruiz, D.J. Braden, J.A. Dumesic, J. Catal. 266 (2009) 71–78.
[7] A.J. Crisci, H. Dou, T. Prasomsri, Y. Román-Leshkov, ACS Catal. 4 (2014) 4196–4200.
[8] J.Q. Bond, A.A. Upadhye, H. Olcay, G.A. Tompsett, J. Jae, R. Xing, D.M. Alonso, D. Wang, T. Zhang, R. Kumar, A. Foster, S.M. Sen, C.T. Maravelias, R. Malina, S.R.H. Barrett, R. Lobo, C.E. Wyman, J.A. Dumesic, G.W. Huber, Energy Environ. Sci. 7 (2014) 1500–1523.
[9] R. Martinez, M.C. Huff, M.A. Barteau, J. Catal. 222 (2004) 404–409.
[10] R. Pestman, A. van Duijne, J.A.Z. Pieterse, V. Ponec, J. Mol. Catal. A 103 (1995) 175–180.
[11] R. Pestman, R.M. Koster, A. van Duijne, J.A.Z. Pieterse, V. Ponec, J. Catal. 168 (1997) 265–272.
[12] K.M. Dooley, A.K. Bhat, C.P. Plaisance, A.D. Roy, Appl. Catal. A 320 (2007) 122–133.
[13] R.W. Snell, B.H. Shanks, ACS Catal. 3 (2013) 783–789.
[14] F.C. Calaza, T.-L. Chen, D.R. Mullins, Y. Xu, S.H. Overbury, Catal. Today 253 (2015) 65–76.
[15] S.H. Hakim, B.H. Shanks, J.A. Dumesic, Appl. Catal. B 142–143 (2013) 368–376.
[16] T.N. Pham, D. Shi, D.E. Resasco, Top. Catal. 57 (2014) 706–714.
[17] T.N. Pham, D. Shi, D.E. Resasco, J. Catal. 314 (2014) 149–158.
[18] O. Nagashima, S. Sato, R. Takahashi, T. Sodesawa, J. Mol. Catal. A 227 (2005) 231–239.
[19] A. Pulido, B. Oliver-Tomas, M. Renz, M. Boronat, A. Corma, ChemSusChem 6 (2013) 141–151.
[20] H. Bayahia, E.F. Kozhevnikova, I.V. Kozhevnikov, Appl. Catal. B 165 (2015) 253–259.
[21] A.V. Ignatchenko, J.S. DeRaddo, V.J. Marino, A. Mercado, Appl. Catal. A 498 (2015) 10–24.
[22] M.A. Hasan, M.I. Zaki, L. Pasupulety, Appl. Catal. A 243 (2003) 81–92.
[23] M.J.L. Gines, E. Iglesia, J. Catal. 176 (1998) 155–172.
[24] S. Wang, K. Goulas, E. Iglesia, J. Catal. 340 (2016) 302–320.
[25] A.V. Ignatchenko, E.I. Kozliak, ACS Catal. 2 (2012) 1555–1562.
[26] W. Li, H. Huang, H. Li, W. Zhang, H. Liu, Langmuir 24 (2008) 8358–8366.
[27] S. Xie, E. Iglesia, A.T. Bell, Chem. Mater. 12 (2000) 2442–2447.
[28] H. Zhang, J.F. Banfield, Chem. Rev. 114 (2014) 9613–9644.
[29] W. Piskorz, J. Gryboś, F. Zasada, S. Cristol, J.-F. Paul, A. Adamski, Z. Sojka, J. Phys. Chem. C 115 (2011) 24274–24286.
[30] W. Piskorz, J. Gryboś, F. Zasada, P. Zapała, S. Cristol, J.-F. Paul, Z. Sojka, J. Phys. Chem. C 116 (2012) 19307–19320.
[31] G. Kresse, J. Furthmuller, J. Comput. Mater. Sci. 6 (1996) 15–50.
[32] G. Kresse, J. Furthmuller, Phys. Rev. B 54 (1996) 11169–11186.
[33] G. Kresse, J. Hafner, Phys. Rev. B 47 (1993) 558–561.
[34] G. Kresse, J. Hafner, Phys. Rev. B 49 (1994) 14251–14269.
[35] J.P. Perdew, K. Burke, M. Ernzerhof, Phys. Rev. Lett. 77 (1996) 3865–3868.
[36] J.P. Perdew, K. Burke, M. Ernzerhof, Phys. Rev. Lett. 78 (1997), 1396–1396.
[37] P.E. Blochl, Phys. Rev. B 50 (1994) 17953–17979.
[38] G. Kresse, D. Joubert, Phys. Rev. B 59 (1999) 1758–1775.
[39] H.J. Monkhorst, J.D. Pack, Phys. Rev. B 13 (1976) 5188–5192.
[40] U. Diebold, Surf. Sci. Rep. 48 (2003) 53–229.
[41] F. Birch, Phys. Rev. 71 (1947) 809–824.
[42] G. Makov, M.C. Payne, Phys. Rev. B 51 (1995) 4014–4022.
[43] X. Wu, M.C. Vargas, S. Nayak, V. Lotrich, G. Scoles, J. Chem. Phys. 115 (2001) 8748–8757.
[44] S. Grimme, S. Ehrlich, L. Goerigk, J. Comp. Chem. 32 (2011) 1456–1465.
[45] G. Henkelman, H.A. Jonsson, J. Chem. Phys. 113 (2000) 9978–9985.
[46] H.A. Jonsson, G. Mills, K.W. Jacobsen, Nudged Elastic Band Method for Finding Minimum Energy Paths of Transitions, World Scientific, 1998.
[47] G. Henkelman, H.A. Jonsson, J. Chem. Phys. 111 (1999) 7010–7022.
[48] D.A. McQurrie, Statistical Mechanics, University Science Books, Sausalito, CA, 2000.
[49] P. Deshlahra, E. Iglesia, J. Phys. Chem. C 118 (2014) 26115–26129.
[50] E.J. Grootendorst, R. Pestman, R.M. Koster, V. Ponec, J. Catal. 148 (1994) 261–269.
[51] Y. Chiang, M. Hojatti, J.R. Keeffe, A.J. Kresge, N.P. Schepp, J. Wirzt, J. Am. Chem. Soc. 109 (1987) 4000–4009.
[52] A. Mattsson, L. Österlund, J. Phys. Chem. C 114 (2010) 14121–14132.
[53] L.-F. Liao, C.-F. Lien, J.-L. Lin, Phys. Chem. Chem. Phys. 3 (2001) 3831–3837.
[54] F.C. Meunier, D. Tibiletti, A. Goguet, D. Reid, R. Burch, Appl. Catal. A 289 (2005) 104–112.
[55] C.M. Kalamaras, P. Panagiotopoulou, D.I. Kondarides, A.M. Efstathiou, J. Catal. 264 (2009) 117–129.
[56] J. Zhang, M. Li, Z. Feng, J. Chen, C. Li, J. Phys. Chem. B 110 (2006) 927–935.
[57] D. Hibbitts, E. Iglesia, Acc. Chem. Res. 48 (2015) 1254–1262.